Two-dimensional Kagome Materials: Theoretical Insights, Experimental Realizations, and Electronic Structures

Zhongqin Zhang[1,2,†], Jiaqi Dai[1,2,†], Cong Wang[1,2], Hua Zhu[1,2], Fei Pang[1,2], Zhihai Cheng[1,2] and Wei Ji[1,2,*]

[1]*Beijing Key Laboratory of Optoelectronic Functional Materials & Micro-Nano Devices, School of Physics, Renmin University of China, Beijing 100872, China*

[2]*Key Laboratory of Quantum State Construction and Manipulation (Ministry of Education), Renmin University of China, Beijing 100872, China*

*Emails: wji@ruc.edu.cn (W.J.)

ABSTRACT:

In recent years, kagome materials have attracted significant attention due to their rich emergent phenomena arising from the quantum interplay of geometry, topology, spin, and correlations. However, in the search for kagome materials, it has been found that bulk compounds with electronic properties related to the kagome lattice are relatively scarce, primarily due to the hybridization of kagome layers with adjacent layers. Therefore, researchers have shown increasing interest in the construction of two-dimensional (2D) kagome materials, aiming to achieve clean kagome bands near the Fermi level in monolayer or few-layer systems. Substantial advancements have already been made in this area. In this review, we summarize the current progress in the construction and development of 2D kagome lattices. We begin by introducing the geometric and electronic structures of the kagome lattice and its variants. This is followed by a discussion on the experimental realizations and electronic structure characterizations of 2D kagome materials. Finally, we provide an outlook on the future development of 2D kagome lattices.

Keywords: kagome materials, two-dimensional, monolayer, few-layer, kagome bands, spin frustration

1. Introduction

A kagome lattice is a crystal structure made up of interlaced triangles and hexagons. Its intriguing electronic properties, including unique band structures and spin frustration, make it an ideal platform for exploring novel phenomena such as electronic correlations, topological effects and quantum magnetism[1,2]. Research on kagome systems has made significant progress, revealing various novel phenomena, including superconductivity[3–5], charge density waves[6–8], and magnetic Weyl semimetals[9–12], which has greatly fueled interest in exploring kagome materials.

However, researchers found that materials with kagome properties are relatively rare. For example, theoretical predictions indicate that out of 3742 known materials with kagome networks, only about 7% exhibit properties related to the kagome lattice[13]. One reason for this difficulty is that kagome lattices are inherently two-dimensional (2D) structures, yet past research has focused primarily on three-dimensional bulk materials. In these bulk materials, the kagome layers are often covered by other layers[3,10,13,14], and interlayer interactions tend to hybridize the kagome layers with others[3,10], pushing the kagome bands away from the Fermi level or even causing them to disappear[13,14]. Therefore, in pursuit of cleaner kagome systems, researchers have shown increasing interest in 2D kagome materials.

A direct approach to constructing 2D kagome lattices involves fabricating monolayer counterparts of kagome materials, such as monolayer AV_3Sb_5 (A = Cs, K, Rb) and monolayer Nb_3X_8 (X = Cl, Br, I). Theoretical predictions suggest that these monolayers possess novel physical properties[15–17]. However, in practice, both direct exfoliation and molecular beam epitaxy (MBE) growth have encountered technical challenges, and thus, successful synthesis these monolayers remain underexplored[18,19]. In contrast, constructing kagome lattices directly within 2D systems, independent of well-studied bulk kagome materials, represents another significant direction. Given the substantial progress in this area, we believe it is time for a comprehensive, interim review.

This review will present the current advancements in the construction and characterization of 2D kagome materials, with a primary focus on experimental progress while also addressing theoretical explanations and some predictions. First, we will introduce the structure and band characteristics of kagome lattices and their variants. Next, we will sequentially summarize the progress and challenges in constructing 2D kagome lattices in organic systems on surfaces, inorganic systems on surfaces, moiré systems, and superatom systems formed from mirror twin boundaries, presented in the chronological order of their development within the field of two-dimensional kagome materials. Additionally, we will propose a universal strategy for constructing kagome lattices from triangular lattices. Finally, we will offer an outlook on the future development of 2D kagome systems.

2. Kagome lattices and theoretical models

The kagome lattice has various structural variants[20–26], some of which can significantly modify the band structure. Therefore, this section introduces the structural evolution from the regular kagome lattice to its various variants and how these changes affect their band structures.

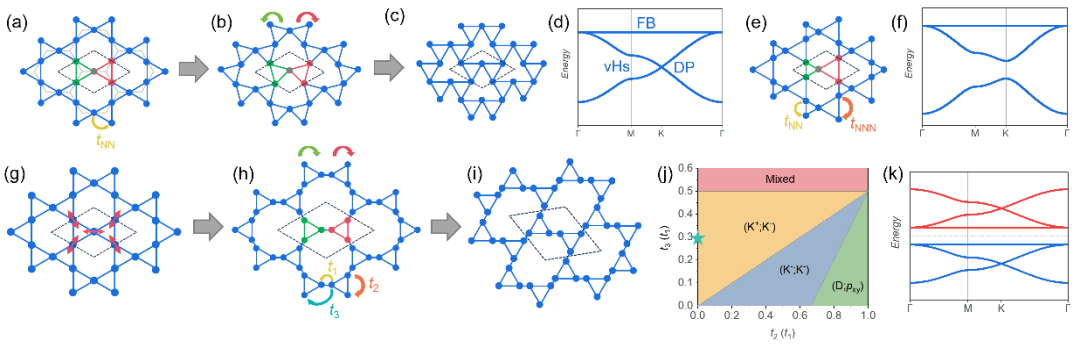

Figure 1 Structure and tight-binding bands of kagome lattices. (a-d) Schematic illustrations of the structures for the regular kagome lattice (a), twisted kagome lattice (b), and coloring-triangle lattice (c), along with their corresponding band structure (d). In (a), t_{NN} represents the nearest-neighbor hopping constant. In (b), the arrows indicate the rotation direction of the corresponding colored

triangles in the unit cell. (e-f) Schematic illustrations of the structure (e) and bands (f) of the breathing kagome lattice. In (e), t_{NN} and t_{NNN} represent the nearest-neighbor and next-nearest-neighbor hopping constants, respectively. The band structure shown in (f) corresponds to t_{NN}/t_{NNN} = 1.5. (g-k) The structural evolution from the regular kagome lattice (g) to the diatomic kagome lattice (h) and chiral diatomic kagome lattice (i), along with the phase diagram of bands (j) and a band structure [t_3/t_1 = 0.3 and t_2 = 0, corresponding to the parameters at the star in (j)] (k). In (h), t_1, t_2, and t_3 represent the hopping constants; the arrows indicate the rotation direction of the corresponding colored triangles in the unit cell. The dashed line represents the Fermi level when the on-site energy is zero in the tight-binding calculation, and different colors in the band structure indicate two sets of kagome bands. The black dashed lines in the structural schematic diagrams represent the unit cell.

In Figure 1a, the gray lines outline a two-dimensional honeycomb lattice. If the single gray lattice point in the honeycomb lattice is replaced by three blue lattice points arranged as shown in Figure 1a, the resulting lattice composed of the blue points forms a regular kagome lattice. The regular kagome lattice consists of two corner-sharing triangles, marked in blue and red in Figure 1a. If we consider only and the nearest-neighbor hopping between them, the tight-binding Hamiltonian can be expressed as follows:

$$H(k) = \begin{pmatrix} 0 & 2t\cos k_1 & 2t\cos k_2 \\ 2t\cos k_1 & 0 & 2t\cos k_3 \\ 2t\cos k_2 & 2t\cos k_3 & 0 \end{pmatrix}$$

where $k_n = \boldsymbol{k} \cdot \boldsymbol{a}_n$, with $\boldsymbol{a}_n$ representing the displacement vectors between the nearest neighbors in the kagome lattice. Solving this Hamiltonian yields the band structure shown in Figure 1d, which features three key characteristics: a flat band (FB) spanning the Brillouin zone, a Dirac point (DP) at the K point, and two van Hove singularities (vHSs) at the M points. When these unique electronic features are near the Fermi level, they can impart novel properties to the materials. The flat band in the kagome lattice arises from the destructive quantum interference of the wave functions, making it a topological flat band. In this flat band, the suppression of kinetic energy

makes the Coulomb interactions relatively more prominent, leading to their dominance over the system's physical properties. As a result, the flat band in the kagome lattice introduces electronic correlations, leading to a range of novel physical phenomena. For instance, experiments have shown that the ferromagnetic ground state in Fe_3Sn_2 originates from correlation effects enhanced by the flat band[27]. The Dirac fermions impart topological properties to materials[28], such as magnetic Weyl semimetal phase in $Co_3Sn_2S_2$[9–12]. And the vHSs can also introduce strong electronic correlations and lead to Fermi surface nesting, which in turn may cause instabilities in the Fermi surface. Such instabilities have been observed in CsV_3Sb_5, where the competition between charge density waves, superconductivity, and other long-range orders has been reported[5,6,29]. These unique kagome band structures and the resulting physical phenomena make the kagome lattice an ideal platform for studying the interplay of electronic correlations, topology, and magnetism. However, it is important to note that the tight-binding model discussed above considers only a single orbital at each lattice point and nearest-neighbor hopping between them. If more orbitals, more complex symmetries of orbitals, or longer-range hopping interactions are taken into account, the shape of the bands will change[30].

If the two triangles, colored red and blue in the regular kagome lattice, each rotate around their centers (as indicated by the arrows in Figure 1b), the resulting structure is a twisted kagome lattice (Figure 1b). If both triangles rotate by exactly 30° in opposite directions, the lattice becomes the coloring-triangle (CT) lattice (Figure 1c). Theoretically, it has been shown that both the twisted kagome lattice and the CT lattice are equivalent to the regular kagome lattice, sharing the same band structure (Figure 1d) [25,26]. The breathing kagome lattice (Figure 1e) introduces further structural complexity by breaking the size (interaction) equivalence of the two corner-sharing triangles. This symmetry breaking causes the two Dirac bands, which were originally degenerate at the K (Dirac) point, to split, thereby opening a band gap.

When each lattice point in the regular kagome lattice is split into two distinct points (Figures 1g, h), the resulting structure is called a diatomic kagome lattice[23,24]

(Figure 1g). This lattice can also be understood as the two triangles in the regular kagome lattice being pulled apart, causing their shared corner points evolving into two separate points. This variant has more complex hopping dynamics, and depending on the relative magnitudes of the three near-neighbor hopping constants, it can result in several different band structures, as illustrated in the phase diagram in Figure 1j. Notably, in the (K+, K-) region of the phase diagram (shaded in yellow), the band structure features two sets of kagome bands, with the flat bands positioned adjacent to each other. When the Fermi level lies between these two flat bands, theoretical calculations predict that this unique "yin-yang" flat band structure can facilitate the realization of phenomena such as excitonic insulators[31] and the quantum anomalous Hall effect[32]. Furthermore, by rotating the two triangles within the unit cell of the diatomic kagome lattice (marked by blue and red triangles in Figure 1h), different chiral diatomic kagome lattices can be obtained, one of which is shown in Figure 1i. The chiral diatomic kagome lattice does not change the fundamental band structure of the diatomic kagome lattice[33–35]. This provides a degree of tolerance for material imperfections, allowing the realization of the kagome band properties even in materials that do not have a perfectly ordered diatomic kagome lattice.

The different types of kagome lattices introduced above can also be combined to form new structures, such as the breathing chiral diatomic kagome lattice[33], which exhibits a band structure that combines the characteristics of both the breathing kagome lattice and the diatomic kagome lattice.

Currently, the regular kagome lattice, twisted kagome lattice, CT lattice, and breathing kagome lattice have all been realized in two-dimensional systems with atomic structures. However, the diatomic and chiral diatomic kagome lattices have only been demonstrated in electronic structures and have yet to be realized in atomic structures, requiring further research and development.

3. Organic kagome monolayers on surfaces

Organic molecules, due to their diverse structures, flexible assembly, and tunable functionalities, are playing an increasingly important role in the design and creation of low-dimensional materials. Researchers can precisely control the shape and size of molecules, as well as the type and position of their functional groups, and use them as building blocks to construct complex surface lattice structures through methods like surface supramolecular self-assembly and surface chemical reactions[36–41]. To date, dozens of organic lattices have been successfully synthesized on solid surfaces. Depending on the bonding interactions between the building blocks, these lattices can be categorized into hydrogen-bonded organic frameworks (HOFs), metal-organic frameworks (MOFs), and covalent organic frameworks (COFs) and others.

Over the past two decades, bottom-up experimental synthesis of organic kagome lattices has made significant progress. Additionally, theoretical calculations have predicted that various intriguing states and phenomena may be realized in freestanding monolayer organic kagome lattices, such as superconductivity[42], the quantum anomalous Hall effect[43], excitonic insulators[31], topological insulators[44,45], and quantum spin liquids[46], offering potential material platforms for exploring novel quantum states.

This section will introduce two primary bottom-up approaches to constructing monolayer kagome lattices on surfaces using organic molecules: the direct approach, which involves linking organic monomers on solid-liquid interfaces or vacuum-solid surfaces to directly form lattice networks with the molecules themselves, creating atomic kagome lattices; and the indirect approach, where organic molecules form repulsive barriers that spatially confine the surface electronic states of metal substrates, leading to the formation of electronic kagome lattices.

3.1. Surface-supported organic kagome networks

The construction process of organic kagome monolayers on surfaces typically progresses from solid-liquid interface to ultra-high vacuum (UHV)-metal surface, transitioning from weakly bonded self-assembly to strongly bonded structures that require chemical reactions, *i.e.* moving from simpler to more complex methods. This subsection will also broadly follow this step-by-step progression to discuss the development of organic kagome lattices. Finally, this subsection will discuss the challenges in the synthesis, electronic characterization, and tuning and application of the physical properties of organic kagome lattices.

3.1.1. Solid-liquid interfaces

Compared to ultra-high vacuum metal surfaces, the growth conditions for growing two-dimensional organic crystals at solid-liquid interfaces are less demanding. As a result, kagome lattices with various bonding types were often first synthesized at solid-liquid interfaces[40,47,48].

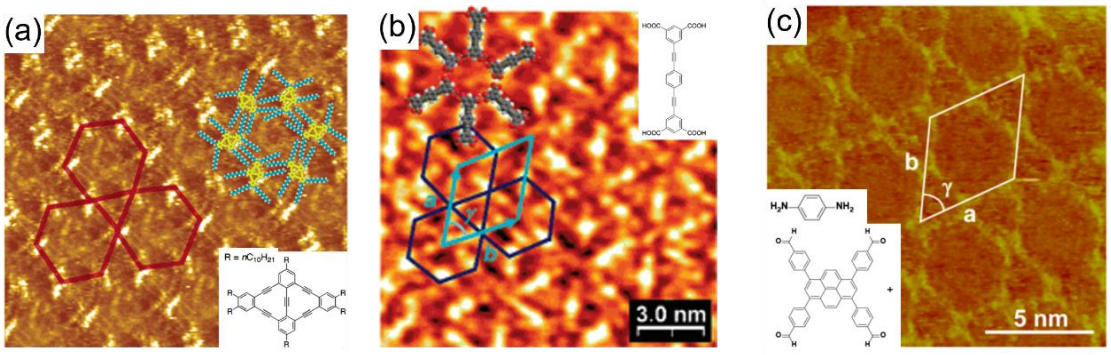

Figure 2 (a) STM image of a kagome network formed by DBA derivatives (inset at bottom right) under ambient conditions. I_{set} = 0.5 nA, V_{bias} = -1.04 V. The scan area is 20.0 × 20.0 nm^2. The molecular model of the building block is overlaid on the STM image to aid visualization. The red lines highlight the kagome symmetry. (b) STM image of a kagome lattice constructed from 5,5'-(1,4-Phenylenedi-2,1-ethynediyl)bis(1,3-benzenedicarboxylic acid) molecules (inset at bottom

right). I_{set} = 50 pA, V_{bias} = -1.5 V. The unit cell is outlined with blue lines, and a molecular model of the building block is overlaid on the STM image to aid visualization. The black lines highlight the kagome symmetry. (c) STM topography image of a kagome network formed by the condensation of p-phenylenediamine molecules and 1,3,6,8-tetrakis(p-formylphenyl)pyrene molecules (inset) under ambient conditions. V = 700 mV, I = 500 pA. (a) Reproduced from Ref.[40], (b) Reproduced from Ref.[48], (c) Reproduced from Ref.[47].

Van der Waals (vdW) interactions are widespread among moleucles and often govern their assembly pattern. The first organic kagome network was also assembled through vdW interactions in 2006. Feyter, Tobe and coworkers used a rhombic derivative of dehydrobenzo[12]annulene (DBA) (inset of Figure 2a) as the building block at the solid-liquid interface of 1,2,4-trichlorobenzene (TCB) and highly oriented pyrolytic graphite (HOPG). Through van der Waals interactions between the molecules, they self-assembled the first molecular aggregate with a two-dimensional kagome lattice, which was confirmed by scanning tunneling microscopy (STM) under ambient conditions at the solid-liquid interface[40] (Figure 2a).

Hydrogen bonding is the most crucial non-covalent interaction in the self-assembly of two-dimensional crystal engineering. In 2007, using 5,5'-(1,4-Phenylenedi-2,1-ethynediyl)bis(1,3-benzenedicarboxylic acid) (as shown in the inset of Figure 2b), Wuest and coworkers synthesized and characterized the first hydrogen-bonded organic framework (HOF) with a kagome lattice at the HOPG solid-liquid interface[48].

In cases where stronger bonding between molecules is involved—such as covalent bonding—the high stability of the bonded molecules often leads to poor crystallinity, making it challenging to form long-range ordered crystals[49]. Despite extensive efforts to synthesize 2D covalent kagome lattices[50], it was not until 2017 that the first monolayer covalent organic framework (COF) kagome lattice was synthesized at a solid-liquid interface using dynamic covalent bonds[47]. Wang and coworkers mixed 1,3,6,8-tetrakis(p-formylphenyl)pyrene and p-phenylenediamine (as shown in the inset

of Figure 2c) in a solvent and deposited the mixture onto the HOPG surface. The resulting kagome network, formed through a Schiff base reaction between the two molecules, was imaged using STM under ambient conditions, as shown in Figure 2c.

3.1.2. Vacuum-metal interfaces

While synthesizing two-dimensional kagome lattices at solid-liquid interfaces is relatively simple, studying their properties presents certain challenges. Many surface characterization techniques, such as STM, often have lower resolution at the solid-liquid interface compared to ultra-high vacuum environments (as shown in Figure 2), and some techniques cannot be applied at the solid-liquid interface at all. However, physicists are primarily interested in the band structure and spin-related phenomena of kagome lattices. To explore and utilize the unique properties of kagome lattices more deeply, researchers have expanded the synthesis environment to metal surfaces in ultra-high vacuum environments. This subsection will discuss the advances of synthesizing organic kagome lattices on ultra-high vacuum metal surfaces and the study of their electronic properties, including self-assembly through van der Waals forces, hydrogen bonds, and covalent bonds between organic molecules, as well as the introduction of metal atoms to form metal-organic coordination bonds between molecules.

3.1.2.1. VdW-bonded kagome networks

The first organic kagome network at vacuum-metal interfaces was also assembled via vdW interactions. In 2008, Barth, Ruben, Schlickum and coworkers deposited a series of linear dicarbonitrile-polyphenyl molecules (lower right inset of Figure 3a) on an Ag(111) surface. Under UHV STM, they discovered that the NC-Ph_5-CN molecules self-assembled into a kagome lattice through van der Waals forces (Figure 3a) [51], marking the beginning of research on organic kagome monolayers on metal surfaces in ultra-high vacuum environments. Additionally, the triangles forming the kagome lattice, influenced by the polarity of the cyanogroups (CN groups) in the NC-Ph_5-CN

molecules, underwent slight rotations, resulting in a chiral molecular structure (upper right inset of Figure 3b), which is a common phenomenon in organic kagome systems[52]. However, this chirality arises from the structural chirality of the molecules themselves and does not necessarily correspond to the chiral diatomic kagome lattices discussed in the previous section at the electronic structure level.

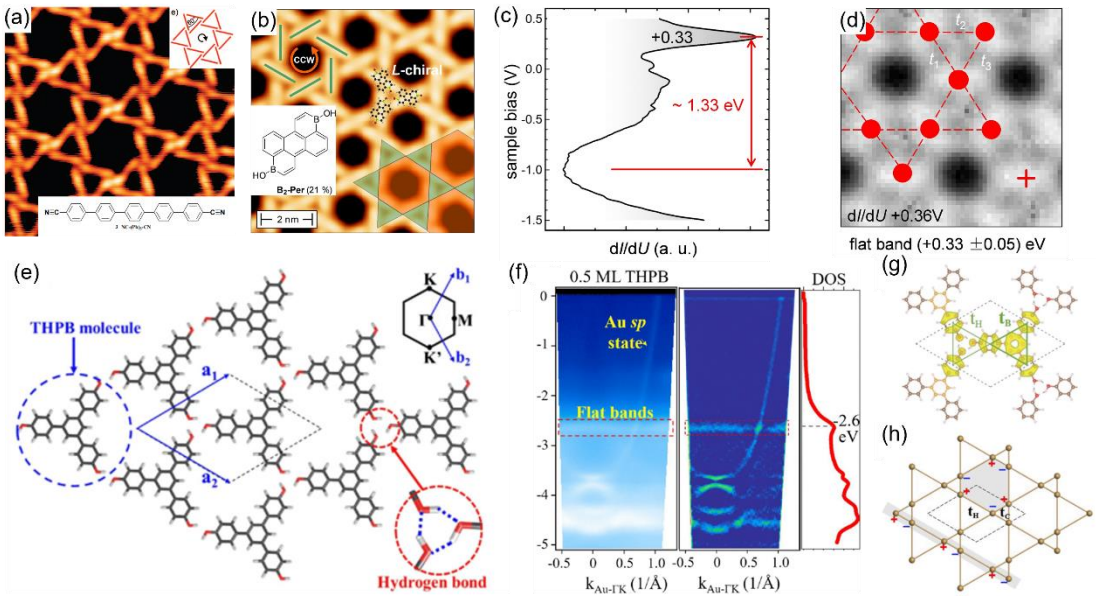

Figure 3 (a) STM image of a kagome network formed by NC-Ph_5-CN (inset at bottom right). I = 0.1 nA, V = 0.5 V. (b-d) STM image (b), *dI/dV* spectra (c), and *dI/dV* map at 0.36 V (d) of the kagome lattice constructed by B_2-Per. In (b), U = 1 V, CCW indicates counterclockwise; the atomic model of building blocks is overlaid on the STM image; green and orange shading represent the triangles and hexagons of the kagome lattice, respectively. In (d), the kagome lattice and lattice points are overlaid on the *dI/dV* map, with the red cross in the bottom right indicating the position where the *dI/dV* spectra were taken. (e-h) (e) Schematic model of the kagome lattice formed by THPB. (f) ARPES spectrum of a 0.5 ML THPB film along the Γ-K_{Au} direction (left), second-derivative plot (middle), and the integrated DOS from the ARPES (right). (g) The optimized lattice structure overlaid with partial charge density derived from the top three valence bands belonging to the breathing-kagome lattice formed by CBRs of THPB. The brown or orange, red, and pink balls represent C, O, and H atoms, respectively. The charge density is plotted using an isosurface of 0.002 eV/Å^3. (h) Illustration of an electronic breathing-kagome lattice formed by different hopping strength of t_H via H bonds versus t_C via covalent bonds [see also (g)], as if there were breathing

bonds of different lengths. (a) Reproduced from Ref. [51], (b-d) Reproduced from Ref. [53], (e-h) Reproduced from Ref. [54].

3.1.2.2. Hydrogen-bonded kagome networks

The electronic coupling strength of hydrogen bonds is relatively weak, often leading to a large bandgap in HOFs[55,56]. As a result, even when a kagome lattice is formed, it is challenging to achieve kagome bands near the Fermi level. To address this issue, Perepichka, Liu and coworkers proposed the concept of donor-acceptor hydrogen-bonded organic frameworks (DA HOFs). Through first-principles calculations, they demonstrated that appropriately designed hydrogen-bond interactions could significantly enhance charge transfer and donor/acceptor abilities of the molecules by stabilizing/destabilizing their LUMO/HOMO, thereby reducing the bandgap of the compound and enabling the formation of a flat band with a bandwidth of less than 0.06 eV near the Fermi level. The authors also explored the possibility that partial filling of this flat band could induce Stoner ferromagnetism[57]. Experimentally, Qi, Würthner, Haldar and coworkers used 3,9-diboraperylene diborinic acid derivative B_2-Per as building blocks (shown in the inset of Figure 3b) and deposited them on an Ag(111) surface under ultra-high vacuum, where they found that B_2-Per molecules self-assembled into a kagome lattice[53], as shown in Figure 3b. Scanning tunneling spectroscopy (STS) measurements of this system revealed an enhanced density of states at 0.33 eV above the Fermi level (Figure 3c), and the *dI/dV* map at 0.36 eV (Figure 3d) indicated that this peak is related to the kagome flat band. The researchers confirmed through a tight-binding model that the organic system corresponds to a regular kagome lattice with a hopping constant of t = 0.44 eV.

Interestingly, researchers found that organic molecular systems can exhibit a phenomenon where the molecular structure forms a regular kagome lattice, but due to varying ease of electron transfer in different points of the lattice, the electronic band structure exhibits characteristics of a breathing kagome lattice in HOFs[54]. Pan, Liu, Li, Gao and coworkers deposited 1,3,5-tris(4-hydroxyphenyl)benzene (THPB) molecules

on an Au(111) surface. These THPB molecules self-assembled into HOFs, where the corner benzene rings (CBRs) of the molecules formed a kagome lattice (Figure 3e). Angle-resolved photoemission spectroscopy (ARPES) measurements revealed a flat band with an energy of -2.6 eV over the whole Brillouin zone (Figure 3f), marking the first direct observation of a flat band in reciprocal space within a monolayer material. Theoretical calculations indicated that in this kagome system, when electrons hop between kagome lattice points, they have two possible pathways. Electrons can either hop within the THPB molecules through covalent bonds or hop between THPB molecules through hydrogen bonds. Each type of hopping corresponds to different hopping constants, as shown in Figure 3g. By fitting the results of density functional theory (DFT) calculations using a tight-binding breathing kagome lattice Hamiltonian, the researchers identified an intramolecular hopping constant t_C = 0.26 eV and an intermolecular hopping constant t_H = 0.05 eV. Thus, despite the similar lattice point distances (d_C = 7.4 Å and d_H = 7.2 Å), the differing hopping paths lead to the formation of a distinct electronic breathing kagome lattice (Figure 3h), which results in the kagome flat band observed in ARPES measurements.

3.1.2.3. Covalently bonded kagome networks

When organic molecules are covalently bonded, stronger bonding can enhance intermolecular hybridization, allowing electrons to delocalize beyond the individual building blocks. This delocalization increases the intermolecular hopping constants, thereby making it more probable for COFs to form kagome bands near the Fermi level. Researchers proposed and predicted that using building blocks with D_{3h}[58]or C_3[59] symmetry to construct COFs with kagome lattices could lead to a range of intriguing physical phenomena, such as Dirac semimetals[58], high-mobility semiconductor carriers[58], and second-order topological insulators[59]. Subsequently, Contini, Perepichka, Rosei, Gallagher and coworkers successfully grew a mesoscale honeycomb-kagome lattice using tribromotrioxaazatriangulene (TBTANG) molecules (inset of Figure 4a) on Au(111) under ultra-high vacuum conditions (Figure 4a). They

observed Dirac cones (Figure 4b) and a flat band 1.8 eV below the Fermi level with ARPES[60]. However, since honeycomb lattices can also contribute Dirac cones, the exact origin of the observed Dirac cones in the experiment remains unclear. As mentioned in the previous section, the strong bonding in COFs presents a challenge for achieving large-area, long-range ordered growth[61], which remains a critical issue to overcome for COFs with kagome lattices in the future.

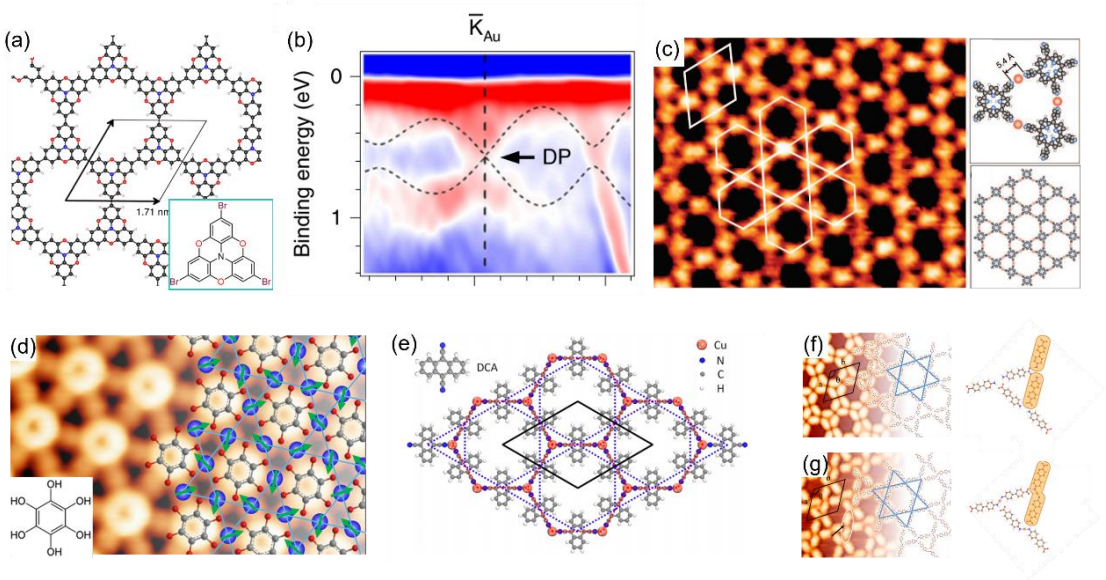

Figure 4 (a) Atomic structure of a kagome lattice constructed by TBTANG molecules (inset). (b) Second derivative plot of the spectrum for PBTANG/Au(111). (c) STM image of a kagome network formed by Au-TPyP (right). I = 0.3 nA, U = -1.3 V. The white lines indicate the unit cell and kagome symmetry. The right panel shows the structural model of the building block and the kagome network, with N, C, H, and Au atoms represented by blue, gray, white, and orange spheres, respectively. (d) STM topography image of a kagome lattice formed by benzene-1,2,3,4,5,6-hexaol (inset at bottom left) and Fe atoms, with the atomic structure overlaid on the right. Fe atoms are represented by blue spheres forming the kagome lattice, with arrows indicating the direction of the magnetic moments on the Fe atoms. V = -10 mV, I = 1nA. (e) Atomic structure of DCA_3Cu_2. (f-g) STM images (left) and structural models (right) of two types of kagome networks formed by ABPCA deposited on a Cu(111) surface. C, H, O, and N atoms are represented by gray, white, red, and blue spheres, respectively. I_t = 100 pA, V_b = -1 V. Scan area is 10 × 10 nm^2. (a-b) Reproduced from Ref. [60], (c)

Reproduced from Ref. [62], (d) Reproduced from Ref. [63], (e) Reproduced from Ref. [64], (f-g) Reproduced from Ref. [65].

3.1.2.4. Metal-coordination-bonded kagome networks

In addition to kagome lattices constructed purely from organic molecules, metal atoms can also be introduced into organic systems to form metal-organic frameworks (MOFs). Metal coordination bonds possess relatively high cohesive energies (0.2–2 eV) compared with other non-covalent interactions, are reversible, and exhibit directionality and selectivity[66]. Moreover, the inclusion of metal atoms endows MOFs with a range of interesting properties, attracting significant attention in chemistry, physics, materials science, and other fields[66–69]. The synthesis of MOFs differs from other bonding interactions; it is generally easier to synthesize and prepare MOFs under ultra-high vacuum conditions than at solid-liquid interfaces, primarily due to solvent effects. In solution, metal ions are protected by their counterions and the solvent sphere, making on-surface coordination challenging, as it requires the replacement of counterions by molecular ligands at the interface, a process that is often complex. As a result, the growth of MOFs at solid-liquid interfaces is more challenging and less developed, and most MOFs have been developed in ultra-high vacuum environments[66], so kagome MOFs are not included in Section 3.1.1.

In 2009, Lin and coworkers synthesized the first surface MOF kagome lattice by depositing 5,10,15,20-tetra(4-pyridyl)porphyrin (TPyP) molecules (Figure 4c, upper right panel) on an Au(111) surface using organic-beam evaporation. In-situ STM observations showed that after annealing the TPyP molecules on the Au(111) surface at 250°C, they formed a kagome lattice structure, as shown in the left panel of Figure 4c[62]. The researchers proposed a structural model depicted in the lower right panel of Figure 4c. In this model, adjacent TPyP molecules are connected by a single Au atom (upper right structural diagram) forming a kagome lattice (lower right structural diagram) with a lattice constant of 4.1±0.1 nm. Similar experiments on Cu(111) and

Ag(111) surfaces did not result in the formation of kagome lattices by TPyP molecules, which the authors attributed to the specific coordination properties of Au atoms.

The metal atoms in MOFs can be magnetic, making the magnetism within MOF-based kagome systems a topic of extensive exploration[70–73]. If magnetic atoms form a kagome lattice, such a system could serve as an platform for studying frustrated magnetism. Lin, Zhao and coworkers deposited benzene-1,2,3,4,5,6-hexaol molecules (inset on the left side of Figure 4d) and Fe atoms sequentially on an Au(111) surface. STM observations revealed a triangular lattice formed by the benzene-1,2,3,4,5,6-hexaol molecules and a kagome lattice formed by the Fe atoms, as shown in Figure 4d[63]. Theoretical calculations indicated that the Fe ions are at a high spin state of S = 2 and are coupled antiferromagnetically. The energy of considered antiferromagnetic configurations was found to be the same, indicating a highly degenerate in-plane ground state. Additionally, STS measurements detected a global spin excitation at 6 meV. The authors suggested that if Fe(II) were replaced with Cu(II), the system could become a candidate for a quantum spin liquid system.

The strong correlation characteristics of kagome lattices can also be observed in MOFs. Schiffrin and coworkers deposited dicyanoanthracene (DCA) molecules (inset of Figure 4e) and Cu atoms on an Ag(111) surface, constructing a DCA_3Cu_2 net, where the DCA molecules formed a kagome lattice, as shown in Figure 4e. STS measurements revealed the Kondo effect within the DCA_3Cu_2 network. After comparing theoretical calculations with experimental results, the authors concluded that the strong correlation effects caused by the intrinsic kagome geometry induces magnetism in the DCA_3Cu_2 system, which then interactes with the metallic substrate to produce the Kondo effect[74]. Besides these examples, MOF-based kagome lattices have been predicted to host a variety of interesting physical phenomena, such as topological insulators[44], Chern insulators[75], multiple Hall effects[76], and superconductivity[42,77], which await experimental realization. Given the limited space, these are not discussed in detail here.

3.1.2.4. Multi-interaction-bonded kagome networks

Beyond single bonding interactions, some researchers have combined two or more types of bonding interactions to construct molecular kagome lattices, resulting in systems that demonstrates better thermodynamic stability compared to those constructed with a single interaction[65,78,79]. For instance, Chi, Li and coworkers deposited 4-aminobiphenyl-4'-carboxylic acid (ABPCA, right structural model in Figure 4f) on a Cu(111) surface under ultra-high vacuum conditions at 300K and found that ABPCA molecules formed an HOFs kagome network through N-H···O hydrogen bonds (Figure 4f) [65]. However, after annealing at 450K, the amino groups of two ABPCA molecules underwent a dehydrogenation reaction, forming N-Cu-N metal coordination bonds, leading to a structural phase transition and the formation of the kagome network shown in Figure 4g, where both hydrogen bonds and metal coordination bonds coexist. This heat treatment altered the bonding interactions between molecules, thereby changing the bond strength and degree of hybridization, providing a simple method to tune the hopping constants between different lattice points in organic kagome systems.

3.1.3. Molecule-decoupled substrates

Over the past two decades, significant advancements have been made in synthesis methods and characterization techniques, leading to remarkable progress in the study of organic kagome monolayers. However, despite theoretical predictions of various intriguing physical phenomena in organic kagome systems, experimentally observing and validating these phenomena remains challenging. For example, although many theoretical models predict well-defined kagome bands near the Fermi level in organic kagome networks, it has been difficult to observe these bands in systems grown on substrates such as HOPG and metal surface[74,79,80]. Even when these bands are observed, they are often far from the Fermi level[54].

The discrepancy between theoretical predictions and experimental observations primarily arises because theoretical models often do not account for the influence of the substrate, focusing instead on freestanding monolayer organic kagome networks. However, extensive experimental evidence suggests that substrates significantly affect the geometric and electronic structure of these networks. These effects include: 1) the substrate can change the structure of the adsorbed molecular network; 2) hybridization between the (semi)metallic substrate (e.g., noble metal (111) surfaces or HOPG) and the organic molecules can disrupt the intrinsic band structure of the freestanding organic kagome lattice; and 3) the charge doping effect of the substrate can shift band features such as flat bands away from the theoretically predicted energy positions.

The influence of metal substrates leads to substantial differences between theoretical predictions based on freestanding two-dimensional organic kagome lattices and actual experimental results. This discrepancy has driven theoretical work to more thoroughly consider the substrate's impact on the electronic structure of these lattices and has motivated experimental efforts to decouple or weaken the coupling between the organic molecular network and the substrate. In recent years, significant progress has been made in this area. This section will discuss the advancements in the growth and characterization of organic molecules on BN/metal surfaces, graphene/metal surfaces, and other two-dimensional materials, as well as provide an outlook on future developments.

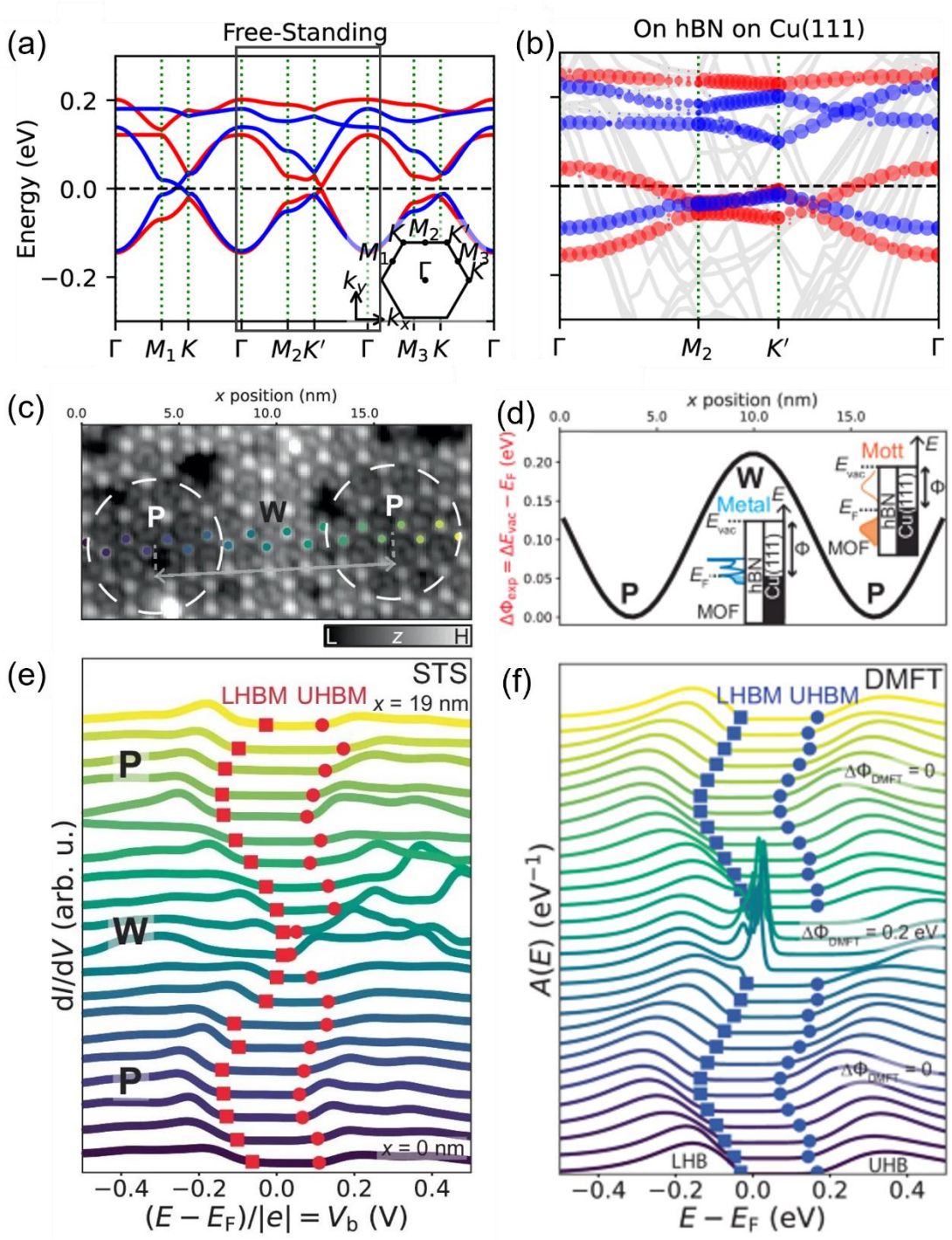

Figure 5 (a-b) Band structure of DCA_3Cu_2 without a substrate (a) and on an h-BN/Cu(111) substrate (b). (c-f) (c) STM image of DCA_3Cu_2 on the h-BN/Cu(111) substrate ($V_b = -1$ V, $I_t = 10$ pA). White dashed circles (P): h-BN/Cu(111) moiré pores, separated by wire (W). Grey arrow indicates moiré period $\lambda \approx 12.5$ nm. (d) Sinusoidal variation of work function, $\Delta\Phi = \Delta E_{vac} - E_F$ (E_{vac}: vacuum energy level), across h-BN/Cu(111) moiré domain with periodicity $\lambda \approx 12.5$ nm, affecting the DCA_3Cu_2 electron filling. (e) *dI/dV* spectra acquired at Cu sites, at positions indicated by colored markers in

(c) (tip 190 pm further from STM setpoint V_b = 10 mV, I_t = 10 pA). Energy gap $E_g \approx 200$ meV at P regions, vanishing at W region (LHBM: lower Hubbard band maximum; UHBM: upper Hubbard band minimum). (f) Spectral functions $A(E)$ calculated via DMFT (U = 0.65 eV, t = 0.05 eV) for isolated uniform DCA_3Cu_2, for different values of E_F. The experimental corrugation $\Delta\Phi$ is accounted for by varying E_F sinusoidally with an amplitude of 0.2 eV, as shown in (d). (a-b) Reproduced from Ref. [81], (c-f) Reproduced from Ref. [82].

Medhekar and coworkers used DFT+U calculations to compare the band structures of freestanding DCA_3Cu_2 (Figure 5a) with those on an h-BN/Cu(111) substrate (Figure 5b). They found that, although the band shape and position of DCA_3Cu_2 on the h-BN/Cu(111) substrate differed slightly from the freestanding case, the changes were minimal, suggesting that h-BN could effectively reduce the coupling between the molecules and the substrate[81]. Afterward, Schiffrin, Medhekar, Powell and coworkers successfully synthesized and characterized the DCA_3Cu_2 kagome system on an h-BN/Cu(111) substrate using STM[82]. The *dI/dV* (Figure 5e) matched well with the spectral function results from dynamical mean-field theory (DMFT) calculations for the freestanding DCA_3Cu_2 network (Figure 5f). This further indicated that, aside from the local work function modulation caused by the moiré pattern of h-BN/Cu(111), molecular decoupling from the metallic substrate was achieved. The study also demonstrated Mott insulating behavior in this system, and local electrostatic control over a Mott metal-insulator-transition. Similarly, inserting a graphene layer between DCA_3Cu_2 and the Ir(111) substrate also achieved molecular-metal substrate decoupling[83]. However, it is important to note that the strength of molecule-substrate interactions varies significantly depending on the specific molecules and substrates used in the process, so whether the results observed from DCA_3Cu_2 are generally applicable remains to be explored in further studies.

In addition to inserting an isolating layer between the molecules and metal substrates, two-dimensional vdW materials, which generally exhibit weak interlayer coupling, can also serve as weakly coupled substrates for growing organic networks.

Liljeroth, Yan and coworkers have grown DCA_3Cu_2 kagome MOF on a two-dimensional vdW superconducting material, $NbSe_2$[84]. If the Cu atoms were replaced with magnetic atoms, the molecular layer could exhibit magnetism, potentially making this system an ideal platform for studying the coupling of magnetism, topology, and superconductivity. Recently, Lin, Huang, Shi and coworkers reported the successful synthesis of a MOF on a two-dimensional vdW semiconductor, MoS_2[85]. Through a comparison of experimental results and theoretical calculations of freestanding organic networks, they found that the molecular structure on the MoS_2 substrate remained consistent with that of the freestanding network. As a vdW material, MoS_2 exerts negligible influence on the organic network's structure. As a semiconductor, MoS_2 may serve as an ideal substrate for preserving the band structure of organic molecules near the Fermi level, offering an potential solution to the molecule-substrate hybridization problem.

However, the catalytic activity of vdW material surfaces is relatively weak, so only systems with weaker bonding, such as the aforementioned metal-organic coordination networks, can be synthesized. These weakly bonded systems tend to localize electrons on the molecules, which is not conducive to forming desired kagome bands near the Fermi level. For systems with stronger intermolecular interactions and hybridization, such as COFs or MOFs formed through metal-organic covalent bonds, further exploration is needed to achieve synthesis on vdW material surfaces. Recently, significant progress has been made in synthesizing large-area, easily transferable COFs at the gas-liquid interface[86,87], suggesting a potential solution: first grow strongly bonded organic kagome networks at the gas-liquid interface, then transfer them onto an insulating substrate for characterization.

3.2. Kagome-structured surface states

As early as the last century, shortly after the advent of STM, scientists began using it to manipulate atoms on metal surfaces, thereby indirectly controlling the surface electronic states of the metal[88]. For example, on a Cu(111) surface, Fe atoms were

manipulated to form a quantum corral, where the quantum confinement effect of Shockley surface states was observed[89]. In recent years, progress has been made in using organic molecules as repulsive potential barriers to confine the electronic states on metal surfaces, leading to the formation of various electronic lattices[90]. Here, this subsection introduces several examples of electronic kagome lattices constructed using organic molecules.

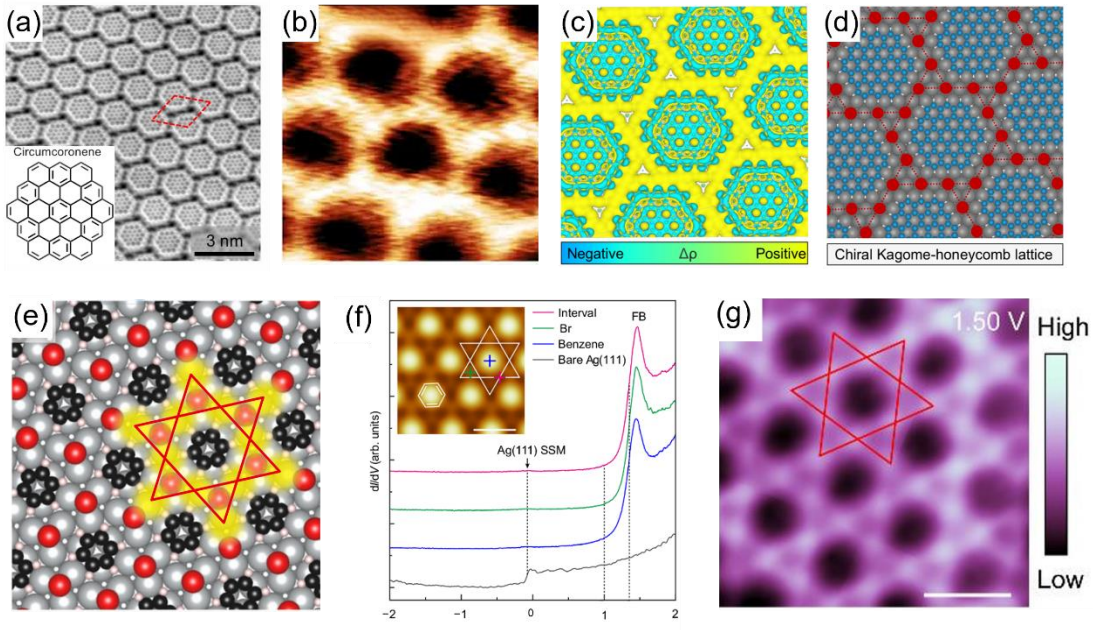

Figure 6 (a-d) Non-contact atomic force microscopy image of a superlattice formed by circumcoronene (inset) (a), *dI/dV* map at 1.15 V (b), electrostatic potential (c), and schematic of the chiral diatomic kagome lattice (d). (e-g) Structural model of the structure of benzene/Br/Ag(111) (e), *dI/dV* spectra (f), and *dI/dV* map at 1.50 V (g). The inset in (f) shows the STM topography image, with the colored-cross indicating the STS measurement position.(a-d) Reproduced from Ref. [35], (e-g) Reproduced from Ref. [33].

In 2021, Lu, Wu, Jelínek and coworkers devise a strategy for the ultrahigh-yield synthesis of circumcoronene molecules on Cu(111) via surface-assisted intramolecular dehydrogenation of the rationally designed precursor, followed by methyl radical-radical coupling and aromatization. They observed that these molecules self-assembled into a triangular lattice on the Cu(111) surface (Figure 6a) [35]. By performing STS

measurements in the gaps between the molecules, the researchers identified two peaks at 0.36V and 1.15V in the *dI/dV* curve , which cannot be explicitly ascribed to tunneling into any frontier molecular orbitals. *dI/dV* maps revealed that the electronic states corresponding to these peaks were primarily located between the molecules (Figure 6b shows the *dI/dV* map at 1.15V). This suggests that the two peaks originate from the surface electronic states of Cu(111). Electrostatic potential calculations (Figure 6c) revealed that the circumcoronene molecules exhibit negative potential, acting as repulsive barriers. This confinement of surface electronic states leads to the formation of an electronic chiral diatomic kagome lattice (Figure 6d) and the emergence of two kagome flat bands.

Recently, Wang, Ma and coworkers proposed a general strategy to construct electronic kagome lattices by on-surface synthesis of halogen hydrogen-bonded organic frameworks (XHOFs) [33]. They successfully realized electronic regular, breathing, and chiral diatomic kagome lattices on brominated Ag(111) and Au(111) surfaces. For example, Figure 6e shows the atomic structure model of the electronic regular kagome lattice, and *dI/dV* spectra in Figure 6f exhibits a peak at 1.5V. The *dI/dV* map at 1.5V (Figure 6g) clearly shows that the surface electronic states between the molecules are arranged in a distinct regular kagome lattice pattern.

Using organic molecules to confine surface electronic states and construct electronic kagome lattices broadens the range of molecules that can be employed, without necessitating the organic network to have a kagome topology. However, this approach also introduces new challenges. Due to the complex interactions between the molecules and the substrate, it is difficult to determine a priori whether the chosen molecules can confine the surface electronic states into a kagome lattice. Additionally, theoretical calculations must thoroughly molecule-substrate interactions, such as the orientation of the molecules relative to the substrate, interfacial stress, and the diverse forms of interfacial coupling, all of which add to the complexity and computational burden. As a result, this method is still in its exploratory stages and requires further in-depth research.

4. Inorganic kagome lattices on surfaces

On surfaces, in addition to constructing kagome lattices with organic molecules, kagome lattices can also be built using atoms or inorganic molecules. This section will introduce advances in this area, including the creation of atomic kagome lattices through templating, as well as the formation of electronic kagome lattices via atomic manipulation, deposition, and orbital hybridization.

4.1. Atomic kagome lattices constructed via surface templates

When a specific structure with kagome-shaped potential wells is formed on a surface, these wells can capture deposited atoms and arrange them into a kagome lattice, allowing for the controlled formation of a single-atom-thick kagome lattice. At this stage, the structure with kagome-shaped potential wells acts as a template for constructing a kagome lattice on the surface. This concept has already been realized by depositing K atoms on a blue phosphorus-gold alloy.

Figure 7a shows a schematic illustration of a blue phosphorus-gold alloy, P_2Au, where two adjacent hexagons provide two potential wells capable of accommodating atoms two adjacent hexagons provide two potential wells capable of accommodating atoms, positioned on the centers of the connecting lines of the nearest neighbor points in a triangular lattice[91,92]. When these two potential wells merge into one (Figure 7b), they form a template for constructing a kagome lattice (indicated by the solid red lines in Figure 7b). Chen, Li, Zhang and coworkers achieved the growth of this single-well blue phosphorus-gold alloy P_4Au_3 by first depositing K atoms on an Au(111) surface under UHV conditions, resulting in the functionalization of the Au(111) surface with K atoms, followed by the deposition of P atoms[93]. STM results (Figure 7c) showed that the K atoms were located within these wells, forming the expected kagome structure.

Additionally, in the blue phosphorus-gold alloy P_2Au (Figure 7a), if only one of the two adjacent potential wells is occupied, it is still possible to construct a kagome

lattice[25]. Du, Zhou, Hao, Zhuang and coworkers synthesized the blue phosphorus-gold alloy P_2Au by first depositing P atoms on an Au(111) surface, then depositing K atoms to occupy the potential wells, thereby constructing a twisted kagome lattice shown in Figures 7d-e. STS measurements revealed a peak in the *dI/dV* spectra, possibly originating from the flat bands of the twisted kagome lattice.

Constructing kagome lattices on surfaces using templates offers a wide range of flexibility, allowing various parameters within the kagome lattice to be tuned by selecting different template shapes, sizes, and materials. However, at the current stage of research, the available templates for constructing kagome lattices remain relatively scarce, limiting the broader application of this approach. Therefore, further development is needed to explore and identify new templates capable of forming kagome potential energy surfaces.

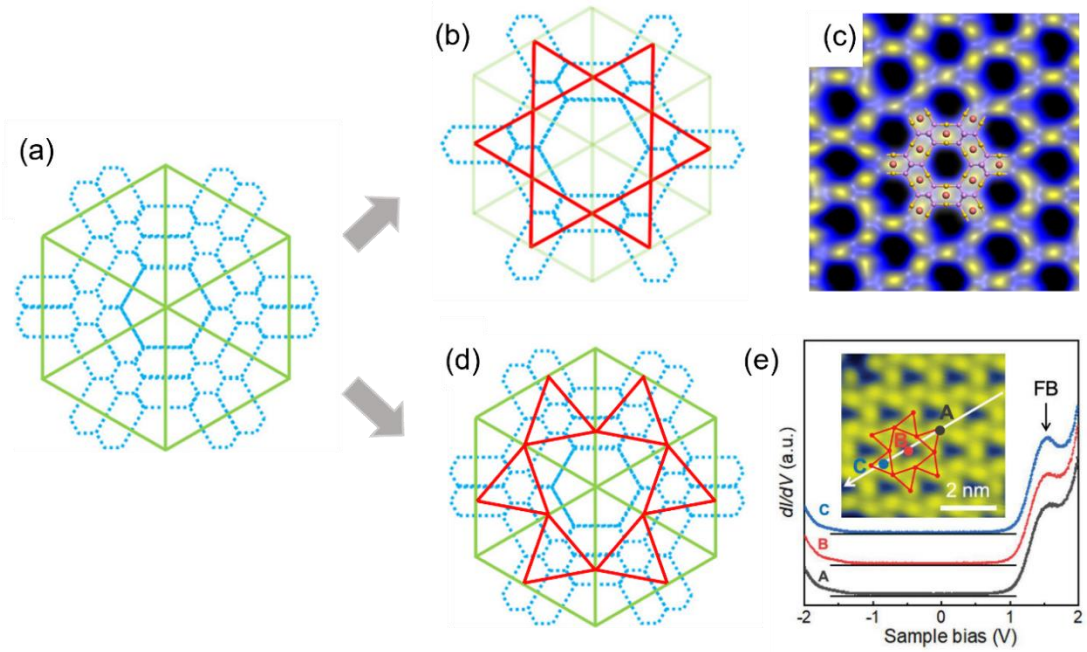

Figure 7 (a) Schematic of the arrangement of the potential wells in P_2Au. (b) Schematic of the single-potential well blue phosphorus-gold alloy P_4Au_3. (c) STM images of potassium-atom-adsorbed P_4Au_3, with the atomic structure overlaid. V_s = -0.02 V. (d) Schematic of a twisted kagome lattice constructed from the double-potential well blue phosphorus-gold alloy P_2Au. (e) Differential conductance spectra of the twisted kagome lattice shown in (d), with the spectra vertically offset for clarity. The underline beneath each spectrum indicates the zero density of states level. The inset

shows an STM image with A, B, and C marking the STS measurement positions. V_s = -0.1 V, I = 200 pA. (a-d) Reproduced from Ref. [93], (e) Reproduced from Ref. [25]

4.2. Atom-scale electronic kagome lattices

Atomic manipulation is a useful method for constructing various lattices. Using this technique, researchers have successfully constructed a series of artificial electronic lattices on Cu(111) surfaces, including honeycomb lattices[94,95], Lieb lattices[96], and kagome lattices[97]. In 2019, Morais Smith, Swart and coworkers used the STM tip to manipulate CO molecules on a Cu(111) surface, arranging them into the structure indicated by the black dots in the inset of Figure 8a. The polar CO molecules induce localized surface potential wells, thereby suppressing the surface states at the adsorption sites. As a result of this confinement effect, the surface electronic states of Cu form a finite-sized breathing kagome lattice, as shown in Figure 8a. The researchers further demonstrated that this finite lattice is a second-order topological insulator with stable zero-energy corner modes (Figure 8b).

One advantage of using tip-based atomic or molecular manipulation to construct lattices is its flexibility, allowing for the customization of various lattice types and the tuning of parameters such as lattice constants and hopping constants, which is crucial for exploring novel quantum effects. However, this method is typically inefficient and lacks scalability. Otte and coworkers developed a kilobyte rewritable atomic-scale memory consisting of 10^4 atoms, based on the self-assembly of Cl atoms on a Cu(100) surface and STM manipulation[98], providing an effective solution to the scalability challenges of atomic manipulation. However, a subsequent challenge arises: the remaining metal surface states may hybridize with the kagome bands or interfere with their observation. Constructing electronic kagome lattices on semiconductor surfaces through atomic manipulation could be a feasible solution [99,100].Recently, Fölsch and coworkers made progress by using the STM tip to manipulate In atoms on the semiconductor InAs(111) surface to create quantum dots, where a peak was observed in the *dI/dV* spectra at -75 meV, corresponding to the quantum dot formed by six In

atoms[101]. Therefore, atomic manipulation on semiconductor surfaces may be an effective way to construct isolated kagome bands near the Fermi level. Additionally, manipulating magnetic atoms on metal[102] or insulator[103] surfaces with an STM tip could also be a promising approach for constructing kagome magnets.

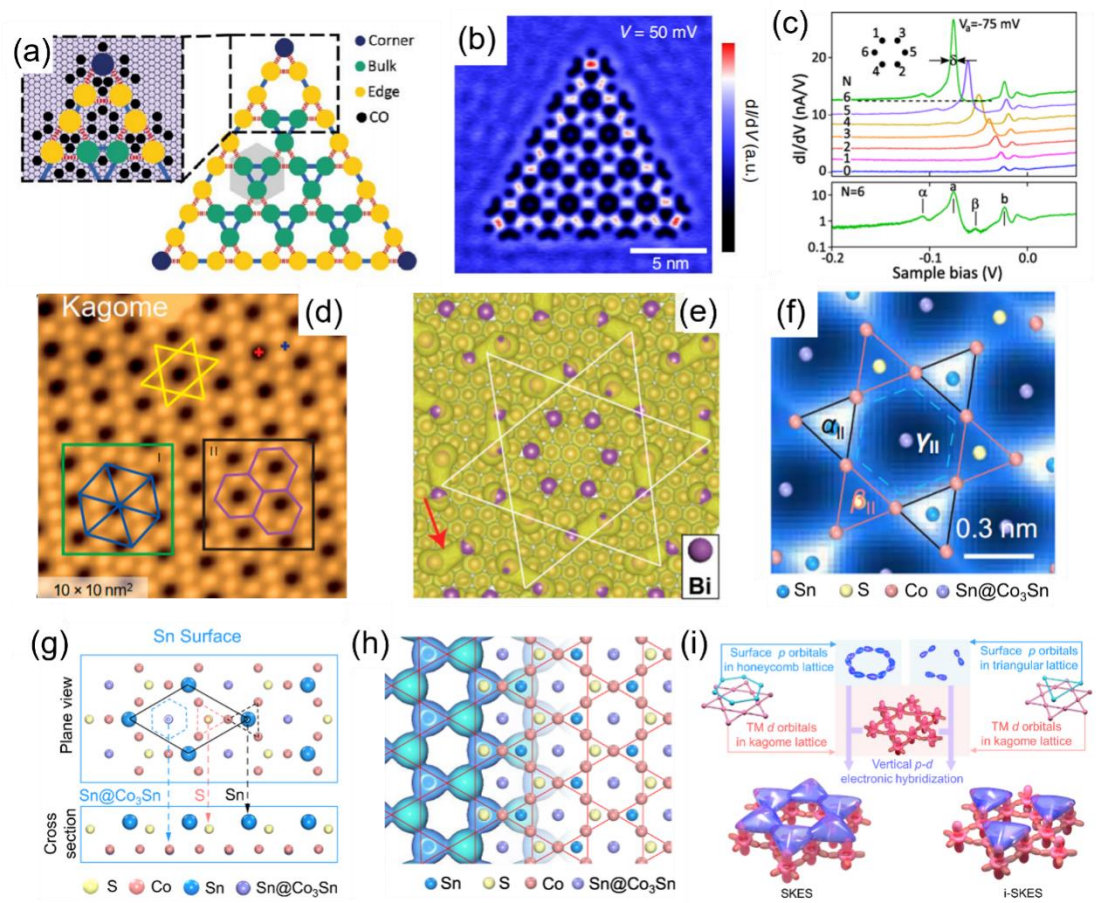

Figure 8 (a-b) (a) Schematic of the kagome lattice formed by CO on a Cu(111) surface (inset) and (b) *dI/dV* map at 50 mV bias. (c) Upper panel: size-dependent *dI/dV* spectra (set point: 1 nA, 0.3 V; V_{mod} = 1.8 mV) with *N* the number of adatoms in the dot (assembly sequence highlighted by the inset): a strong peak evolves at $V_a = -75$ mV for the complete hexagon (*N*= 6) together with smaller peaks at higher and lower energies; the width δ of the main peak (full width at half maximum) is measured relative to the dashed horizontal baseline. Lower panel: logarithmic plot of the *N* = 6 spectrum; peaks denoted α and β are replicas of peaks a and b induced by inelastic electron tunneling. (d) STM image of the kagome lattice formed by Bi on the Au(111) surface. V_s = 1.5 V, I_t = 1000 pA. (e) Atomic structure model of Bi/Au(111) surface and the electronic density distribution. (f-i) (f) Chemical-bond-resolved nc-AFM image of the Type-II surface in $Co_3Sn_2S_2$, the Sn-terminated

surface. Three distinct regions within a unit cell with bright, blurry, and dark contrast, which are marked by black solid line triangles, red solid line triangles, and a blue dashed line hexagon, are labeled as α_{II}, β_{II}, and γ_{II} regions. The atomic structure superimposed is the Sn surface with the underlying S and Co_3Sn plane. (g) DFT optimized surface structure on the Sn surface. (h) Isosurface contour of $|\psi|^2$, integrated from −0.38 eV to the E_F, on the Sn surface superimposed with the atomic structure of the three topmost atomic layers of the Sn surface in the right part. Red solid lines highlight the kagome pattern. (i) Schematic of SKES (the left part) and i-SKES (the right part) formation through vertical *p*–*d* hybridization. (a) Reproduced from Ref. [104], (b) Reproduced from Ref. [97], (c) Reproduced from Ref. [101], (d-e) Reproduced from Ref. [105], (f-i) Reproduced from Ref. [106].

When atoms are directly deposited onto a surface, their interactions with each other and with the substrate can also lead to the formation of electronic kagome lattices. In 2019, Han and coworkers studied the evolution of the self-assembled structures and electronic structures of Bi adatoms on Au(111) surface as the coverage varied. They discovered that when the Bi coverage reached 0.63 ML, the STM images of the Bi adatoms on the surface exhibited a kagome lattice pattern[107]. Later, Qin, Zhang and coworkers also observed the same kagome lattice pattern at a coverage of 0.65 ML, as shown in Figure 8d[105]. Based on first-principles calculations, the researchers proposed a corresponding atomic structure model (Figure 8e). In this model, the Bi atoms are categorized into two types. One type forms dimers with a higher density of electronic states, which appear as bright spots located at the midpoint of the dimers in the STM images, forming a kagome lattice. The other type of Bi atoms resides inside the hexagons of the kagome lattice and appears as dark voids in the STM images. Structurally, the Bi adatoms do not form a kagome lattice, so the observed kagome lattice in the STM images does not reflect the actual atomic arrangement but rather an electronic kagome lattice formed by the electronic states on the Bi dimers (Figure 8e). Additionally, the study revealed that the kagome lattice formed by these Bi dimers creates kagome-shaped potential wells. As a result, when Ge atoms are subsequently

deposited, they tend to occupy positions within the hexagons or triangles of the kagome lattice, forming of a superlattice. This method of forming electronic kagome lattices by depositing atoms onto a surface is straightforward and does not require additional manipulation, but it relies heavily on the choice of specific atoms and substrates. Therefore, it is not yet possible to determine a priori, through experiments and theory, which systems can achieve this structure, and whether a general construction strategy exists remains to be further explored.

Surface kagome electronic states (SKES) can also be constructed based on orbital symmetry through orbital hybridization, and a general strategy was recently proposed by Gao, Ji, Yang and coworkers[106]. This strategy was developed through their studies on the $Co_3Sn_2S_2$ surface. In the $Co_3Sn_2S_2$, there are two types of surfaces: the first type is terminated by a S atom layer, and the second type is terminated by a Sn atom layer. The second surface exhibits properties related to the kagome lattice, such as Weyl fermion arcs, which are not present on the S-terminated surface. Characterization of the second surface using chemical-bond-resolved qPlus non-contact atomic force microscopy (nc-AFM) also revealed a kagome lattice pattern, as shown in Figure 8f. To understand why the Sn-terminated surface exhibits kagome properties, the researchers conducted theoretical calculations. They found that the height difference between the Sn atom layer and the underlying S atom layer is only 0.56 Å in Sn-terminated surface (Figure 8g, side view). These two layers together form a honeycomb lattice (Figure 8g, top view), whose lattice points are directly aligned above the centers of the triangles in the underlying Co_3Sn kagome lattice. Strong hybridization occurs between the *p* orbitals of Sn and S atoms in the honeycomb lattice and the *d* orbitals of Co atoms in the kagome lattice, effectively imprinting the triangular-shaped electronic density of the Co_3 trimers onto those of the surface Sn and S atoms. Subsequently, the *p* orbitals of Sn and S undergo in-plane hybridization, resulting in the formation of a surface electronic kagome lattice on the Sn-terminated surface, as shown in Figure 8h.

Based on the principle of SKES formation on the Sn-terminated surface of $Co_3Sn_2S_2$, the researchers proposed a universal strategy for constructing SKES, as

illustrated in the left panel of Figure 8i: (i) the surface and subsurface (if any) atoms fit in a honeycomb lattice, (ii) their in-plane states vertically hybridize with both of the corner-sharing triangular-shaped sublattices of the kagome lattice underneath, and (iii) their hybridized states then subsequently hybridize laterally with each other to form an SKES, as illustrated in the left part of Fig. 8i. The researchers further validated the universality of this strategy through theoretical calculations of other configurations. For example, replacing Sn with other III-V elements or replacing S with Se or Te consistently resulted in the formation of SKES, confirming the general applicability of the strategy. On the S-terminated surface of $Co_3Sn_2S_2$, only an incomplete SKES (i-SKES) can form because the surface consists solely of a triangular lattice of S atoms, as shown in the right panel of Figure 8i.

5. Moiré kagome few-layers

When two or more two-dimensional layers with lattice mismatch or a twist angle are vertically stacked, they may form a superperiodic structure with a larger period, known as a moiré superlattice. Moiré superlattices can introduce strong correlations or topological properties not present in the original parent two-dimensional materials through mechanisms such as Brillouin zone folding[108,109], structural relaxation[110–112], and interlayer coupling[113,114]. Various intriguing physical phenomena have already been reported in moiré superlattice systems, such as superconductivity and correlated insulators[115–117], moiré excitons[118–120], and the quantum anomalous Hall effect[121,122]. One of the key characteristics of moiré superlattices is their significantly larger real-space period, typically on the order of 10 nm, which is more than an order of magnitude larger than the sub-0.5 nm period of atomic crystals. The significantly increased real-space periodicity effectively reduces the electron density required for tuning band occupancy using gating, thereby expanding the range of tunability. Consequently, if a two-dimensional kagome lattice could be realized within a moiré system, it might be

possible to construct a variety of novel quantum states over a wider tunability range, potentially revealing new and exotic physical effects.

Twisted multilayer silicene is one of the earliest examples of creating electronic kagome lattices in moiré superlattices[123]. As shown in Figure 9a, Du, Hu, Chen and coworkers discovered that the STM images of twisted multilayer silicene with a 21.8° twist angle exhibit a kagome lattice pattern with a period of 1.7 nm. In the *dI/dV* spectra, two narrow peaks were observed above the Fermi level at 1.32 eV and 1.7 eV (Figure 9b). The *dI/dV* map at 1.32V clearly shows a kagome lattice pattern (Figure 10c), indicating the formation of electronic kagome lattice in this system, characterized by extended localized electronic states due to destructive quantum interference.

In addition to twisted silicene, electronic kagome lattices have also been observed in other typical vdW two-dimensional materials with twisted moiré superlattices[124,125]. For instance, similar electronic kagome lattice structures have been found in twisted bilayer WSe_2 with a 5.1° twist angle[125] (Figure 9d) and in twisted bilayer graphene (BG) [124] at angles of 1.07°, 0.98°, and 0.88°.

Atomic kagome lattices have also been observed in twisted moiré systems. In the twisted trilayer graphene system shown in the inset of Figure 9e, with twist angles θ_{12} = 0° and $\theta_{23} \cong 0.06°$, Yoo, Son and coworkers observed kagome-shaped domains using dark field transmission electron microscopy (DF TEM), as shown in Figure 10e[126]. In these domains, the stacking ABC and ACB orders (atomic structures shown on the right side of Figure 9e) form the triangles of the kagome lattice, with alternating bright and dark contrasts in the DF TEM images. However, the origin of this kagome lattice is large-scale atomic structure relaxation at small twist angles, leading to a lattice constant of several hundred nanometers. As a result, the hopping between kagome lattice points is negligible, and it is unlikely that this structure will exhibit kagome properties associated.

Due to the larger lattice constants of moiré superlattices, some microscopy techniques with lower spatial resolution compared to atomic scales can also be effectively utilized. One such technique is scanning microwave impedance microscopy

(MIM) [127–129]. In MIM, microwave signals in the frequency range of 1–10 GHz are guided to a sharp metal tip and projected onto the sample. By analyzing the signals reflected from the sample, the admittance between the tip and the sample can be obtained. The imaginary part of the signal, MIM-Im, increases monotonically with the sample's conductivity, making it useful for measuring the local conductivity of the sample. Zettl, Wang and coworkers used an ultrahigh-resolution implementation of scanning microwave impedance microscopy (uMIM) to image twisted BG/BG/hBN systems (inset of Figure 9f) [130]. They found that, at a twist angle of 0.6°, the low-pass filtered MIM-Im image revealed bright spots, corresponding to high-conductivity domains, arranged in a kagome lattice pattern, as shown in Figure 9f. However, since MIM is sensitive to changes in both atomic structure[130] and electronic structure[128], it remains unclear whether the observed kagome lattice corresponds to an atomic or electronic kagome lattice.

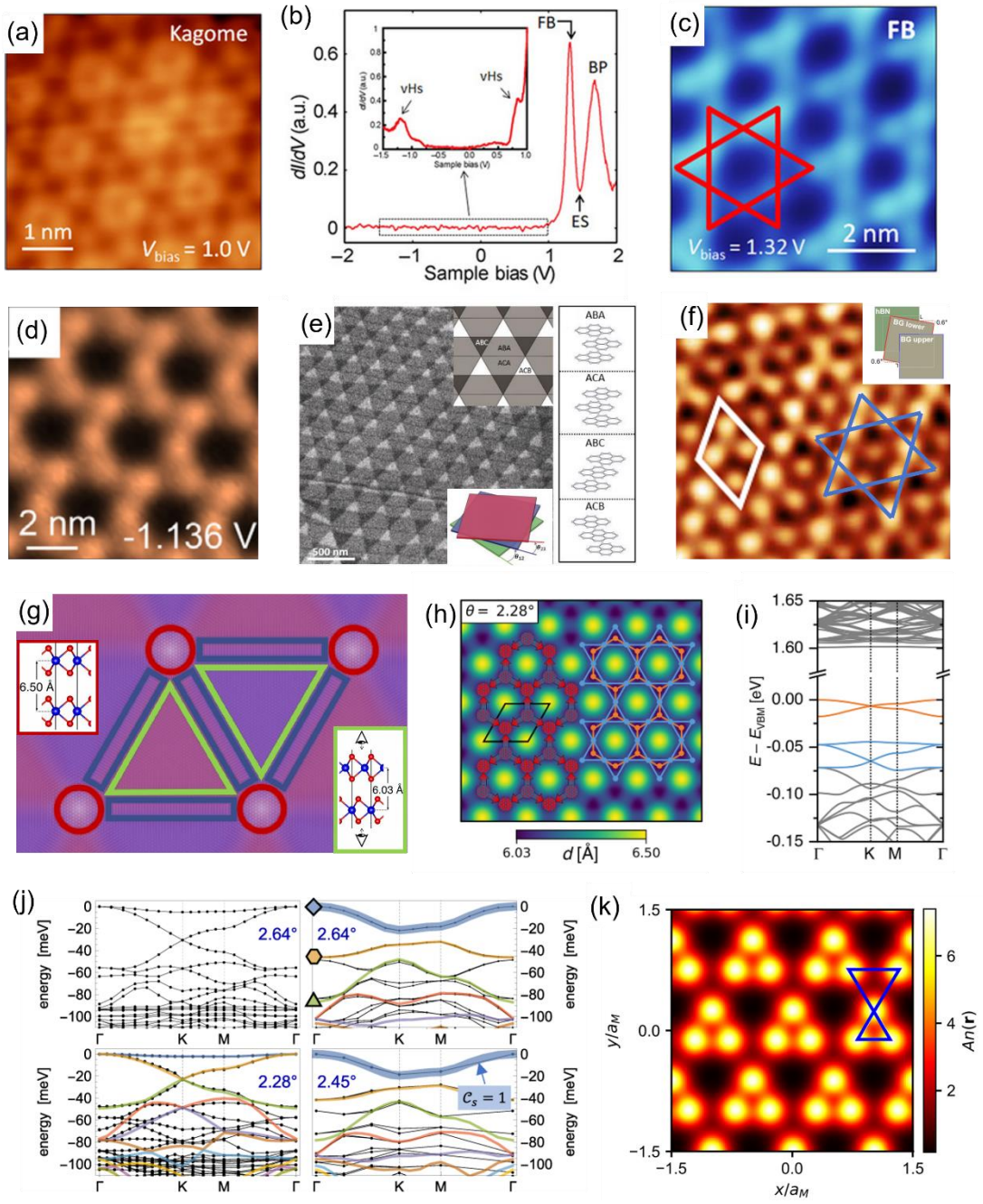

Figure 9 (a-c) STM image (a), *dI/dV* spectra (b), and *dI/dV* map (c) at a bias of 1.32 V of multilayer twisted silicene. In (a), V_s = 1 V, I_t = 100 pA, scan area 5×5 nm^2. (d) *dI/dV* map of 5.1° twisted bilayer WSe_2 at a bias of -1.136 V. (e) DF TEM image of triple-layer twisted graphene with twist angles θ_{12} = 0° and θ_{23} ≅ 0.06° (inset at bottom right). The inset at top right shows the stacking configurations corresponding to the triangular and hexagonal domains of the kagome lattice, with the atomic structure diagrams of different stacking configurations on the right. (f) Low-pass filtered image of the uMIM scan of BG/BG/hBN (inset). (g-h) (g) Fully relaxed atomic structure of twisted bilayer MoS_2 with a twist angle θ = 1.05°. The red circles highlight the R_h^h stacking regions (inset

on the left), the green triangles highlight the R_h^M stacking regions viewed from above or below (inset on the right), and the blue rectangles highlight the solitons. (h) Interlayer separation landscape with a schematic visualization of (left overlay) the structural elements and (right overlay) the superlattices formed by the structural elements in twisted bilayer MoS_2 with a twist angle $\theta = 2.28°$. The R_h^M stacking domains form a honeycomb lattice (orange) while the midpoints of solitons form a kagome lattice (blue). (h) Electronic band structure of twisted bilayer MoS_2 (twist angle $\theta = 2.28°$), calculated at the DFTB level. The bands corresponding to the honeycomb and kagome lattice are highlighted. (j) Ab initio band structure of twisted bilayer ZrS_2, with (right column) and without (left column) spin-orbit coupling, with the top-most valence bands arising from the emergent Kagome lattice. The solid colored lines represent the band structure fitted to the topmost valence band. The thick blue line indicates a topological band with a Chern number of 1. (k) Real-space electron density of a Wigner molecular crystal in a breathing kagome lattice. (a-c) Reproduced from Ref. [123], (d) Reproduced from Ref. [125], (e) Reproduced from Ref. [126], (f) Reproduced from Ref. [130], (g-i) Reproduced from Ref. [131], (j) Reproduced from Ref. [132], (k) Reproduced from Ref. [133].

Although experimental results for kagome lattices in twisted moiré systems are still relatively limited, theoretical predictions suggest that kagome lattices can be realized in various moiré systems. The following examples will illustrate this potential.

Heine, Kuc and coworkers conducted a comprehensive study of the structural and electronic evolutions in twisted bilayer MoS_2 with twist angles ranging from 0.2° to 59.6°. The fully relaxed structure of twisted bilayer MoS_2 is shown in Figure 9g and includes three distinct regions: R_h^h stacking (red circles), R_h^M stacking (green triangles), and solitons (blue rectangles). In the 2.28° twisted bilayer MoS_2, fully relaxed using a reactive force field, the R_h^h stacking region (yellow bright spots in Figure 9h) forms a triangular lattice, while the centers of the solitons (blue spots in Figure 9h) constitute a kagome lattice. The lowest-order density-functional based tight-binding (DFTB) indicates that a clean kagome band structure can be found just 0.05 eV below the Fermi level, as shown by the blue bands in Figure 10i[131]. Similarly, Rubio,

Kennes, Claassen and coworkers, using a semiconductor moiré continuum model[134] and ab initio calculations, predicted distinct kagome bands below the Fermi level in twisted bilayer 1T-ZrS_2 at twist angles of 2.45°, 2.28°, 2.64°, and 3.15° (Figure 9j). These bands are contributed by the degenerate p_x and p_y orbitals of sulfur[132]. Reddy, Devakul, and Fu, using a semiconductor moiré continuum model, predicted that at filling factor n = 3, the Coulomb interaction within each three-electron moiré atom leads to a three-lobed "Wigner molecule". When their size is comparable to the moiré period, the Wigner molecules form an emergent kagome lattice due to the balance between Coulomb interaction and moiré potential, as shown in Figure 9k [133]. These calculations are general predictions for semiconductor moiré systems. Wang, Crommie, Fu and coworkers performed STM imaging of Wigner molecule crystals in a twisted bilayer WS_2 system, but the Wigner molecule size was smaller than the moiré period, so a kagome lattice was not formed[135]. Similarly, twisted bilayer graphene with a twist angle of approximately 1° may also form a Wigner crystal[136], where the lattice of the Wigner crystal changes with the electron filling. At a filling of 3/4, a kagome lattice Wigner crystal could potentially emerge. Apart from twisted moiré systems, Kong, Ji and coworkers predicted that applying different in-plane strains to the layers of an untwisted graphene homo-bilayer could also lead to the emergence of a twisted kagome structure and kagome bands[137].

Although the experimental and theoretical research on kagome lattices in moiré systems has made encouraging progress, several challenges remain to be addressed. Theoretically, for moiré systems with small twist angles, first-principles calculations may require handling more than 10^3 atoms, posing significant challenges for structural relaxation. This makes accurate predictions of the structure and electronic properties of moiré systems difficult, thereby limiting the ability to simulate, predict, and interpret kagome lattices in moiré systems. Experimentally, twisted Moiré systems face challenges related to structural stability, as the twist angle may change under thermal, mechanical, or other perturbations[138–141]. Moreover, research on the characteristics of kagome bands in moiré systems remains insufficient, and the potential advantage of

easily tuning band occupancy through electrostatic gating in these systems has not been fully exploited. Although electronic kagome lattices have been constructed and kagome flat bands have been observed in moiré systems, the specific properties of these flat bands, such as their topological properties, require further exploration. Despite the challenges faced in studying kagome lattices in moiré systems, these challenges also highlight future research directions. Exploring how to fully exploit the advantages of moiré systems and the unique physical phenomena that may arise from the interaction between moiré and kagome lattices are promising and exciting areas for further investigation.

6. Mirror twin boundaries as superatoms for constructing kagome monolayers

In monolayer transition metal dichalcogenides (TMDs), grain boundaries, as a type of structural defect, have a significant impact on the material's thermal, mechanical, electrical, and other properties[142–146]. A notable example is the mirror twin boundary (MTB), which forms between regions with a relative orientation of 60°. To date, three primary MTB structures have been reported in various TMD materials: 4|4P[142], 4|4E[142], and 55|8[147] (Figure 10a-c, respectively). These structures exhibit different electronic properties, but they all introduce relatively isolated in-gap states within the bandgap of the TMDs.

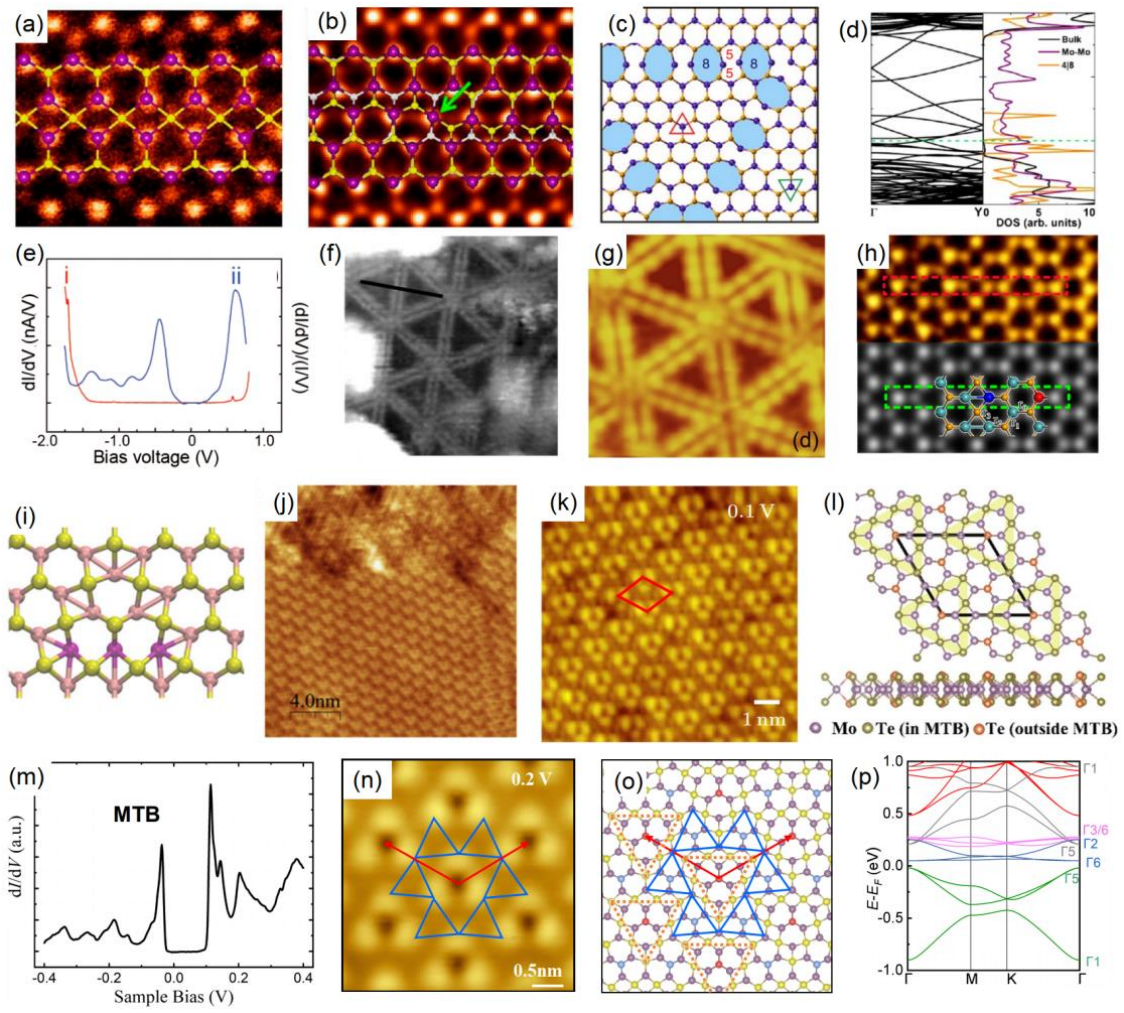

Figure 10. (a-b) Atomic-resolution annular dark-field STEM (ADF-STEM) images of 4|4P and 4|4E 60° grain boundaries in MoS_2, overlaid with atomic structure diagrams of both boundaries. (c) Atomic structures of 55|8 grain boundaries in WSe_2, containing three boundaries composed of 8–5–5–8 membered rings. (d) Band structure and local density of states (LDOS) for the 4|8 grain boundary. (e) *dI/dV* spectra for monolayer (ML) $MoSe_2$ at the interior of the grain boundary (i) and on the MTB triangular loop (ii). (f) STM image of $MoSe_2$ on MoS_2. Size: 23 × 23 nm^2, I_t = 0.20 nA, V_{simple} = -0.78 V. (g) STM image of $MoSe_2$ on HOPG. Size: 13 × 13 nm^2, V_{simple} = 1.46 V. (h) Experimental and simulated ADF images. Scale bar: 0.5 nm. Partial atomic structure diagrams are overlaid. (i) The smallest MTB triangular loop, with three additional Mo atoms highlighted in deep pink. (j-k) $2\sqrt{3}\times2\sqrt{3}$ superlattice in $MoTe_2$, V_b = 500 mV, I_t = 500 pA in (j), I = 100 pA in (k). (l) Atomic structure model of Mo_5Te_8, with the side view shown below. The MTB is marked by yellow triangles. Mo atoms are represented by purple spheres, Te atoms shared by the MTB are shown in green, and Te atoms outside the MTB are shown in orange. (m) The *dI/dV* spectra on the MTB. (n)

STM image of Mo_5Te_8 at a bias of 0.2 V. The coloring-triangular (CT) lattice is highlighted by solid blue lines, and the lattice vectors are marked by red arrows. (o) Atomic structure of Mo_5Te_8, with the MTB highlighted by orange dashed lines. (p) Band structure of Mo_5Te_8. The irreducible representations of the four CT bands at the Γ point are listed on the right, marked in green, blue, purple, and gray. (a-b) and (d) Reproduced from Ref[142], (c) Reproduced from Ref[147], (e) and (g) Reproduced from Ref[148], (f) Reproduced from Ref[149], (h) Reproduced from Ref[150], (i) Reproduced from Ref[151], (j) Reproduced from Ref[152], (k) Reproduced from Ref[153], (l) Reproduced from Ref[154], and (m-p) Reproduced from Ref[20].

In 2013, Zhou and coworkers identified two MTBs in 1H-MoS_2, composed of four-fold rings that share sulfur atoms, known as 4|4P and 4|4E[142]. The lattices on either side of the 4|4P boundary are mirror-symmetric, whereas the 4|4E boundary requires an additional translation. As shown in Figure 10d, theoretical calculations predict that these grain boundaries form one-dimensional metallic quantum wires, with electronic states crossing the Fermi level. In 2014, Xie and coworkers grew $MoSe_2$ samples on HOPG substrates using MBE[148] and experimentally discovered metallic states at the boundaries (Figure 10e). These one-dimensional metallic wires form a characteristic triangular inversion region, which combines into a wheel-like pattern[148] (Figure 10g). This wheel-like structure was proposed to be a result of MTBs sharing, rather than the previously assumed moiré interference effect[149,155–158] (Figure 10f). In 2015, Zhou and coworkers further proposed that in monolayer $MoSe_2$, the grain boundaries of triangular inversion regions are enclosed by MTB loops composed of one-dimensional metallic wires sharing Se atoms[158]. Since then, such metallic wires[155,159] and wheel-like structures[160–162] have been discovered in various MoX_2 (X = S, Se, Te) materials. In 2017, Ji, Jin, Xie and coworkers, using high-resolution ADF-STEM imaging combined with DFT calculations, confirmed that the MTB triangular rings in monolayer $MoSe_2$ correspond to 4|4P MTBs sharing Se atoms[150] (Figure 10h). These in-gap states are typically attributed to the formation of charge ordering, such as Peierls-type charge density waves (CDW)[152,159,163] or Tomonaga-Luttinger

liquids[164,165].

The smallest 4|4P MTB loops require the addition of three extra Mo atoms[151], as shown in Figure 10i. Taking $MoTe_2$ as an example, in 2017, Zhang, Wang and coworkers reported a $2\sqrt{3} \times 2\sqrt{3}$ superlattice on a 2H-$MoTe_2$ sample[152] (Figure 10j, though its exact periodicity was debated, with some initially suggesting a 2×2 superperiodicity[153] (Figure 10k). Later in 2020, Xie, Jin and coworkers definitively identified this structure as a new layered transition metal chalcogenide, Mo_5Te_8[154], featuring a $2\sqrt{3} \times 2\sqrt{3}$ superlattice and the smallest MTB loops, as illustrated in Figure 10l. Further research revealed that Mo_5Te_8 can form coloring-triangle (CT) lattice[20,26], as described in the Section 2. In 2023, Ji, Wang, Cheng and coworkers discovered that this structure possesses electronic band structures similar to those of a kagome lattice, located near the Fermi level (Figure 10m and 10p). The STM topography image clearly shows the CT lattice, as indicated by the blue solid lines in Figure 10n, corresponding to the atomic structure in Figure 10o. The orange dashed lines connect the shared Te atoms on the MTB, with the Mo atoms at the vertices of the triangular regions forming the lattice points of the CT, and the red arrows highlight the $2\sqrt{3} \times 2\sqrt{3}$ superlattice. Each set of the CT bands (CT1-CT4) consists of a "nominally flat band" with minimal broadening, accompanied by two Dirac bands, with irreducible representations indicating their connection through mirror symmetry operations σ_h (Figure 10p).

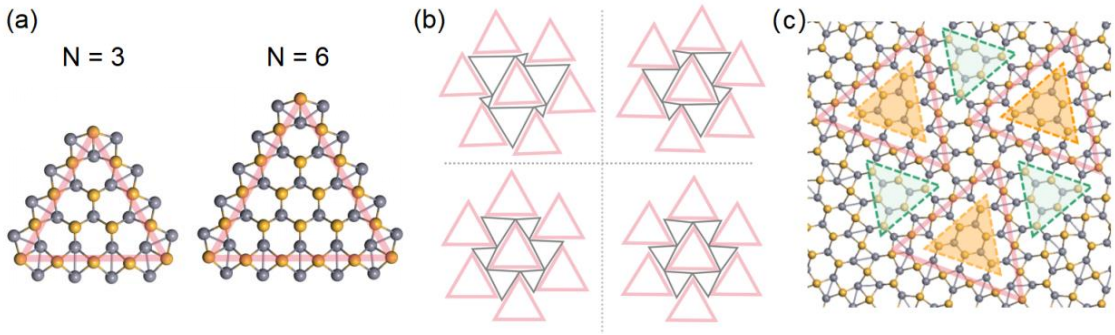

Figure 11: (a) Triangular MTB loops of different sizes in monolayer $MoTe_{2-x}$, with the MTBs highlighted by pink triangles. (b) Various arrangements of MTB loops, with a grid of four (breathing) coloring triangular lattices highlighted with solid black lines connecting the Mo atoms at the vertices. (c) Atomic structure of $Mo_{33}Te_{56}$, with orange and green triangles marking the regions within and

between the MTB loops, respectively.

The MTBs sharing chalcogen atoms can form uniformly sized and well-ordered triangular loops. In 2024, Ji, Zhang and coworkers further investigated MTB superlattices of varying sizes[166]. These triangles can be regarded as superatoms, and depending on their size and arrangement, they have the potential to form kagome lattices or CT lattices. For instance, in $MoTe_{2-x}$, the atomic structures of MTB loops of different sizes are shown in Figure 11a, with the shared Te atoms highlighted in pink triangles. These basic units can theoretically be arranged into various MTB superlattices (Figure 11b), with Mo_5Te_8 being the smallest configurations. For example, in $Mo_{33}Te_{56}$ (Figure 11c), the triangular regions enclosed by orange and green dashed lines collectively form the aforementioned wheel-like pattern, where the "spokes" around the central hexagon correspond to the mirror twin boundaries. This method can construct a kagome lattice capable of producing at least two sets of isolated intrinsic kagome electronic states, similar to the characteristics of Mo_5Te_8. The authors present the formation energies of different configurations. As the chemical potential of Te decreases (from right to left), they identified four stable monolayers across varying chemical potential of Te, while all of them were synthesized in experiments. Zhang, Wu, Yuan, Ji and coworkers investigated the electronic and magnetic properties of $Mo_{33}Te_{56}$[167]. From the non-magnetic band structure, it is evident that when the kagome bands are partially filled, a high density of states at the Fermi level arises, leading to spontaneous magnetization, which can result in the emergence of novel correlated states.

In monolayer H-phase TMDs with chalcogen deficiencies, triangular networks formed by mirror twin boundaries can introduce in-gap electronic states near the Fermi level within the bandgap between the valence and conduction bands. Viewing MTB loops as superatoms and using them as fundamental building blocks, one can construct kagome-like superlattices at the two-dimensional limit, where topological flat bands and Dirac states near the Fermi level can be observed. The variation in the size and arrangement of these MTB loops offers a rich diversity in the resulting superlattices.

Additionally, the kagome bands derived from this method are less prone to hybridization with other bands, resulting in more isolated intrinsic electronic states in these two-dimensional materials. Experimentally, these electronic, magnetic, and topological properties near the Fermi level can be further tuned through gating or other methods, providing a novel avenue for designing kagome materials with specific properties.

7. "1+3" strategy: constructing a kagome lattice from a triangular lattice

Triangular lattices are widely present in two-dimensional materials and on surfaces. This section introduces a "1+3" strategy for constructing a kagome lattice starting from a triangular lattice. As shown in Figure 12a, starting from the 2×2 supercell of a triangular lattice (gray dashed lines), if one of the four lattice points within the supercell (marked in blue) is differentiated from the other three lattice points (marked in pink) through means such as vacancies, substitutions or adsorption, these three pink lattice points form a kagome lattice. Additionally, Figure 12a can be understood in another way: the midpoints (pink points) of the lines connecting the nearest neighbor lattice points in the triangular lattice (blue points) can also form a kagome lattice. The second interpretation is already demonstrated in the kagome lattices formed by Fe atoms in Figure 3d and the potential wells in Figure 7. Next, we will explain this "1+3" strategy in detail through two examples.

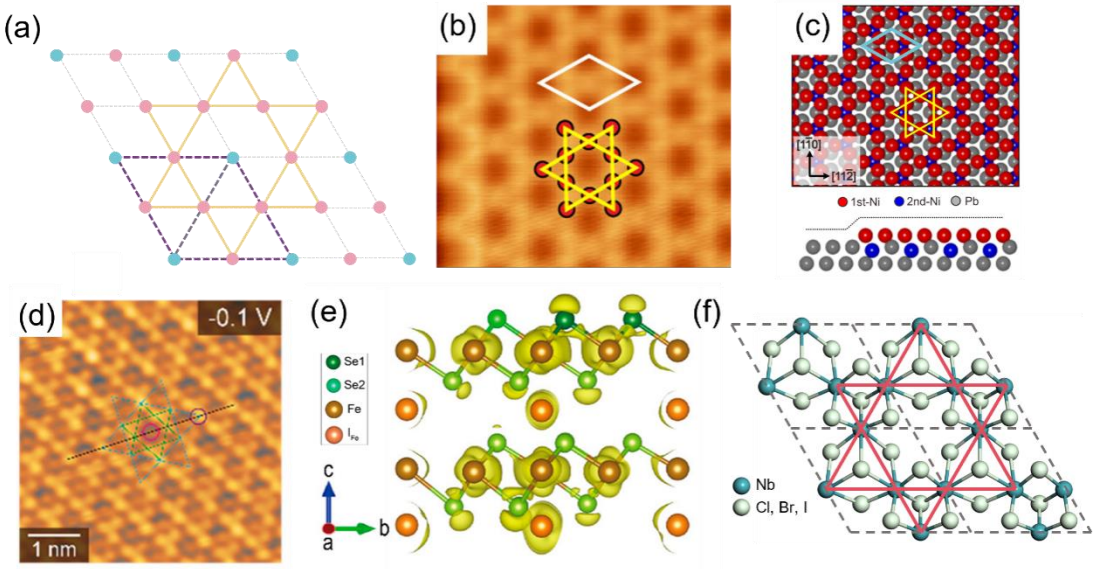

Figure 12 (a) Schematic illustration of constructing a kagome lattice from a triangular lattice. The gray dashed lines represent a 1×1 triangular lattice, the purple dashed lines represent a 2×2 supercell, and the red and blue dots represent different lattices points. The orange solid lines highlight the kagome lattice. (b-c) STM image (b) and atomic structure (c) of Ni deposited on a Pb(111) surface. In (b), U_b = +10 mV, I_t = 1.0 nA. The red dots indicate the kagome lattice formed by the Ni (yellow hexagrams). The white (b) and light blue (c) rhombus outlines the unit cell of the kagome lattice. (d-e) STM image (d) and atomic structure (e) of Fe_5Se_8. In (d), U = -0.1V, I_t = 100 pA, and scan area is 5 × 5 nm^2. The green dashed lines indicate the two periodic kagome lattices observed in the STM image, corresponding to 2×2 and $2\sqrt{3}\times2\sqrt{3}$ structures. In (e), the integrated charge density from -0.5 to -0.3 eV is overlaid on the atomic structure. (f) Atomic structure of Nb_3X_8. (b-c) Reproduced from Ref. [168], (d-e) Reproduced from Ref. [169].

Hsu, Bihlmayer and coworkers deposited Ni atoms on a Pb(111) substrate and observed a kagome lattice in the STM image, as shown in Figure 12b[168]. The line profile extracted from the STM images over the energy range of [-1.0 V, 1.0 V] indicated that the average apparent height of the adatom layer is unusually low about 0.82 Å, suggesting that the mechanism of formation of this kagome lattice might differ from that in Bi/Au(111)(Figure 8e). The atoms on the Pb(111) surface are arranged in a triangular lattice, with atoms in the upper layer positioned over hollow sites of the underlying atomic layer. Theoretical calculations revealed that during deposition, one

of the four Pb atoms in a 2×2 supercell of the top layer is replaced by a Ni atom, creating a "1+3" difference in the hollow sites where Ni atoms can adsorb. The subsequently deposited Ni atoms prefer to adsorb at the hollow sites of the Ni-Pb2 triangles (Figure 12c), leading to the formation of a kagome lattice arrangement of the Ni adatoms on the surface.

If 1/4 or 3/4 of an atomic layer is intercalated between two layers of two-dimensional materials with a triangular lattice, a 2×2 supercell can be formed, potentially leading to the construction of a kagome lattice. Figure 12d shows an example of this concept realized by Zhang, Fu, Liu and coworkers in 1T-$FeSe_2$[169]. As shown in Figure 12e, multilayer $FeSe_2$ is AA stacked, and after intercalating 25% of Fe atoms directly below the Fe atoms in the $FeSe_2$ layer, a 2×2 supercell is formed, resulting in a bulk chemical stoichiometry of Fe_5Se_8. Due to interactions with the intercalated Fe atoms, the surface Se atoms are divided into two types: 3/4 of the Se atoms (Se1) are positioned 0.025 Å higher than the remaining 1/4 of Se atoms (Se2). At this point, the Se1 atoms form a kagome lattice, and the corresponding STM image displays the kagome structure shown in Figure 12d. Besides, DFT calculations reveal that a similar height difference occurs among the Fe atoms in the $FeSe_2$ layer, causing 3/4 of the Fe atoms to form a kagome lattice and generate kagome bands. Similar results have also been reported in a $CoTe_2$ self-intercalation system with the same structure[170].

Constructing kagome lattices starting from T or H phase MX_2-type 2D materials (Janus structures fall under the same category) with a triangular lattice offers a rich degree of freedom for exploring materials and novel physical properties. From a materials perspective, beyond the intercalation-induced formation of M_5X_8 (where M is a metal and X is a group VI or VII nonmetal), various methods can be employed to induce "1+3" differentiation in the 2×2 structure of MX_2. For instance, introducing 1/4 vacancies in the metal layer can form M_3X_8, where the M atoms create a kagome lattice. Examples of such structures include Nb_3X_8 (X=Cl, Br, I) [171] (Figure 12f) and their variants Nb_3TeCl_7[172] and Nb_3SeI_7[19]. Additionally, introducing 1/4 vacancies in the topmost X atom layer can form M_4X_7, where the top X atoms construct a kagome lattice,

as has been experimentally demonstrated in Pt_4Te_7[173,174]. Besides, replacing an atom is similar to creating a vacancy. There are also several conceptual approaches awaiting experimental and theoretical exploration. For example, continuing the intercalation strategy by inserting 3/4 of metal M atoms between layers could form M_7X_8, where the intercalated M atoms would create a kagome lattice. Similarly, inserting 1/4 or 3/4 nonmetal X atoms could form M_4X_9 or M_4X_{11}, or introducing different Y atoms could form $M_4X_8Y_1$ or $M_4X_8Y_3$, where the coupling between the Y atoms and the original layered MX_2 structure might introduce new properties. From the perspective of exploring novel physical properties, selecting appropriate materials and interactions could enable the realization of novel kagome properties. For instance, introducing 3/4 magnetic atoms into semiconductor layered materials might be a promising approach for creating kagome magnets.

The "1+3" strategy is a general approach for constructing kagome lattices from triangular lattices. In addition to the examples mentioned above, kagome lattices can also be constructed through methods such as adsorption[175] and vacancy introduction[176–178], among others, which are not detailed here. Exploring new methods and materials for constructing kagome lattices based on this strategy remains a promising and worthwhile area of research.

8. Outlook

In recent years, research on 2D kagome lattices has rapidly advanced, providing a rich variety of materials for physics research. However, we believe this is merely the beginning, as the future holds vast opportunities and challenges. Reflecting on our original goals in studying 2D kagome materials and looking toward the future, we identify three research directions that are crucial for this field.

First, although two-dimensional atomic or electronic kagome lattices have been realized in various systems, materials with kagome bands near the Fermi level remain scarce. To address this challenge, high-throughput calculations and experimental

screening should be employed to identify potential kagome materials. Additionally, the rapid development of artificial intelligence (AI) offers new pathways for material design. We might develop new design methods to establish correlations between elements, structures, and electronic bands, enabling AI to design ideal, experimentally feasible materials.

Second, synthesis, manipulation, and characterization techniques need further advancement. Phenomena widely explored in bulk kagome materials, such as superconductivity and charge density waves, have yet to be observed in 2D kagome systems. Although many potential systems and methods for constructing 2D kagome lattices have been theoretically predicted[179–185], the feasibility of these predictions and the challenges involved still await experimental validation, highlighting the urgent need for experimental methods to more easily verify theoretical predictions. Moreover, existing measurement techniques also require improvement—for instance, determining whether the observed peaks in STS belong to kagome flat bands and accurately identifying the topological nature of bands using ARPES. Furthermore, the traditional approaches, manipulation methods, and characterization techniques used in bulk materials research need to be adapted and refined for 2D kagome systems.

Finally, the study of spin frustration effects in kagome magnets has long been a focal point in condensed matter physics[186–188]. The relatively flexible construction methods in 2D systems offer unique opportunities to realize kagome magnets and precisely tune key parameters such as spin exchange constants. This provides a promising avenue for exploring and verifying novel phenomena such as quantum spin liquids, making it an attractive and potential-rich research direction.

In summary, two-dimensional kagome lattice materials exhibit immense research potential. As understanding of these materials deepens, we anticipate that this field will attract increasing attention and lead to more groundbreaking discoveries. This review not only summarizes the current state of research on 2D kagome lattices, but also as extends an invitation to the broader scientific community to enjoy the quantum party

held in the kagome lattice, inviting more researchers to join this exciting exploration and contribute to its advancement.

Acknowledgements

We thank Prof. Minghu Pan at Shaanxi Normal University, Prof. Yi Du at Beihang University, Haihui Wang at The Chinese University of Hong Kong and Yunlong Wang at Renmin University of China for valuable discussions. We gratefully acknowledge the financial support from the Ministry of Science and Technology (MOST) of China (Grant No. 2023YFA1406500), the National Natural Science Foundation of China (Grants No. 11974422 and 12104504), the Fundamental Research Funds for the Central Universities, and the Research Funds of Renmin University of China [Grants No. 22XNKJ30] (W.J.). J.D. was supported by the Outstanding Innovative Talents Cultivation Funded Programs 2023 of Renmin University of China.

References

[1] Y. Wang, H. Wu, G. T. McCandless, J. Y. Chan, M. N. Ali, *Nat Rev Phys* **2023**, *5*, 635.
[2] J.-X. Yin, B. Lian, M. Z. Hasan, *Nature* **2022**, *612*, 647.
[3] Y. Hu, X. Wu, B. R. Ortiz, S. Ju, X. Han, J. Ma, N. C. Plumb, M. Radovic, R. Thomale, S. D. Wilson, A. P. Schnyder, M. Shi, *Nat Commun* **2022**, *13*, 2220.
[4] C. C. Zhu, X. F. Yang, W. Xia, Q. W. Yin, L. S. Wang, C. C. Zhao, D. Z. Dai, C. P. Tu, B. Q. Song, Z. C. Tao, Z. J. Tu, C. S. Gong, H. C. Lei, Y. F. Guo, S. Y. Li, *Phys. Rev. B* **2022**, *105*, 094507.
[5] B. R. Ortiz, S. M. L. Teicher, Y. Hu, J. L. Zuo, P. M. Sarte, E. C. Schueller, A. M. M. Abeykoon, M. J. Krogstad, S. Rosenkranz, R. Osborn, R. Seshadri, L. Balents, J. He, S. D. Wilson, *Phys. Rev. Lett.* **2020**, *125*, 247002.
[6] Y. Xu, Z. Ni, Y. Liu, B. R. Ortiz, Q. Deng, S. D. Wilson, B. Yan, L. Balents, L. Wu, *Nat. Phys.* **2022**, *18*, 1470.
[7] S. Cao, C. Xu, H. Fukui, T. Manjo, Y. Dong, M. Shi, Y. Liu, C. Cao, Y. Song, *Nat Commun* **2023**, *14*, 7671.
[8] H. Chen, H. Yang, B. Hu, Z. Zhao, J. Yuan, Y. Xing, G. Qian, Z. Huang, G. Li, Y. Ye, S. Ma, S. Ni, H. Zhang, Q. Yin, C. Gong, Z. Tu, H. Lei, H. Tan, S. Zhou, C. Shen, X. Dong, B. Yan, Z. Wang, H.-J. Gao, *Nature* **2021**, *599*, 222.
[9] N. Morali, R. Batabyal, P. K. Nag, E. Liu, Q. Xu, Y. Sun, B. Yan, C. Felser, N. Avraham, H. Beidenkopf, *Science* **2019**, *365*, 1286.
[10] D. F. Liu, A. J. Liang, E. K. Liu, Q. N. Xu, Y. W. Li, C. Chen, D. Pei, W. J. Shi, S. K. Mo, P. Dudin, T. Kim, C. Cacho, G. Li, Y. Sun, L. X. Yang, Z. K. Liu, S. S. P. Parkin, C. Felser, Y. L. Chen, *Science* **2019**, *365*, 1282.
[11] E. Liu, Y. Sun, N. Kumar, L. Muechler, A. Sun, L. Jiao, S.-Y. Yang, D. Liu, A. Liang, Q. Xu, J. Kroder, V. Süß, H. Borrmann, C. Shekhar, Z. Wang, C. Xi, W. Wang, W. Schnelle, S. Wirth, Y. Chen, S. T. B. Goennenwein, C. Felser, *Nature Phys* **2018**, *14*, 1125.
[12] Q. Wang, Y. Xu, R. Lou, Z. Liu, M. Li, Y. Huang, D. Shen, H. Weng, S. Wang, H. Lei, *Nat Commun* **2018**, *9*, 3681.
[13] M. Jovanovic, L. M. Schoop, *J. Am. Chem. Soc.* **2022**, *144*, 10978.
[14] S. Gao, S. Zhang, C. Wang, S. Yan, X. Han, X. Ji, W. Tao, J. Liu, T. Wang, S. Yuan, G. Qu, Z. Chen, Y. Zhang, J. Huang, M. Pan, S. Peng, Y. Hu, H. Li, Y. Huang, H. Zhou, S. Meng, L. Yang, Z. Wang, Y.

Yao, Z. Chen, M. Shi, H. Ding, H. Yang, K. Jiang, Y. Li, H. Lei, Y. Shi, H. Weng, T. Qian, *Phys. Rev. X* **2023**, *13*, 041049.
[15] K. Nakazawa, Y. Kato, Y. Motome, *Phys. Rev. B* **2024**, *110*, 085112.
[16] Y. Zhang, Y. Gu, H. Weng, K. Jiang, J. Hu, *Phys. Rev. B* **2023**, *107*, 035126.
[17] S.-W. Kim, H. Oh, E.-G. Moon, Y. Kim, *Nat Commun* **2023**, *14*, 591.
[18] S. Park, S. Kang, H. Kim, K. H. Lee, P. Kim, S. Sim, N. Lee, B. Karuppannan, J. Kim, J. Kim, K. I. Sim, M. J. Coak, Y. Noda, C.-H. Park, J. H. Kim, J.-G. Park, *Sci Rep* **2020**, *10*, 20998.
[19] J.-P. Wang, X. Chen, Q. Zhao, Y. Fang, Q. Liu, J. Fu, Y. Liu, X. Xu, J. Zhang, L. Zhen, C.-Y. Xu, F. Huang, A. J. Meixner, D. Zhang, G. Gou, Y. Li, *ACS Nano* **2024**, *18*, 16274.
[20] L. Lei, J. Dai, H. Dong, Y. Geng, F. Cao, C. Wang, R. Xu, F. Pang, Z.-X. Liu, F. Li, Z. Cheng, G. Wang, W. Ji, *Nat Commun* **2023**, *14*, 6320.
[21] H. Liu, S. Meng, F. Liu, *Phys. Rev. Materials* **2021**, *5*, 084203.
[22] Y. Zhou, G. Sethi, H. Liu, Z. Wang, F. Liu, *Nanotechnology* **2022**, *33*, 415001.
[23] Y. Zhou, G. Sethi, C. Zhang, X. Ni, F. Liu, *Phys. Rev. B* **2020**, *102*, 125115.
[24] W. Jiang, X. Ni, F. Liu, *Acc. Chem. Res.* **2021**, *54*, 416.
[25] Y. Li, S. Zhai, Y. Liu, J. Zhang, Z. Meng, J. Zhuang, H. Feng, X. Xu, W. Hao, M. Zhou, G. Lu, S. X. Dou, Y. Du, *Advanced Science* **2023**, 2303483.
[26] S. Zhang, M. Kang, H. Huang, W. Jiang, X. Ni, L. Kang, S. Zhang, H. Xu, Z. Liu, F. Liu, *Phys. Rev. B* **2019**, *99*, 100404.
[27] Z. Lin, J.-H. Choi, Q. Zhang, W. Qin, S. Yi, P. Wang, L. Li, Y. Wang, H. Zhang, Z. Sun, L. Wei, S. Zhang, T. Guo, Q. Lu, J.-H. Cho, C. Zeng, Z. Zhang, *Phys. Rev. Lett.* **2018**, *121*, 096401.
[28] G. Xu, B. Lian, S.-C. Zhang, *Phys. Rev. Lett.* **2015**, *115*, 186802.
[29] F. H. Yu, D. H. Ma, W. Z. Zhuo, S. Q. Liu, X. K. Wen, B. Lei, J. J. Ying, X. H. Chen, *Nat Commun* **2021**, *12*, 3645.
[30] S. Okamoto, N. Mohanta, E. Dagotto, D. N. Sheng, *Commun Phys* **2022**, *5*, 1.
[31] G. Sethi, Y. Zhou, L. Zhu, L. Yang, F. Liu, *Phys. Rev. Lett.* **2021**, *126*, 196403.
[32] F. Chen, J. Lu, X. Zhao, G. Hu, X. Yuan, J. Ren, *Applied Physics Letters* **2024**, *125*, 043103.
[33] R. Yin, X. Zhu, Q. Fu, T. Hu, L. Wan, Y. Wu, Y. Liang, Z. Wang, Z.-L. Qiu, Y.-Z. Tan, C. Ma, S. Tan, W. Hu, B. Li, Z. F. Wang, J. Yang, B. Wang, *Nat Commun* **2024**, *15*, 2969.

[34] X. Li, D. Wang, H. Hu, Y. Pan, *Nanotechnology* **2024**, *35*, 145601.
[35] M. Telychko, G. Li, P. Mutombo, D. Soler-Polo, X. Peng, J. Su, S. Song, M. J. Koh, M. Edmonds, P. Jelínek, J. Wu, J. Lu, *Sci. Adv.* **2021**, *7*, eabf0269.
[36] J. Mao, H. Zhang, Y. Jiang, Y. Pan, M. Gao, W. Xiao, H.-J. Gao, *J. Am. Chem. Soc.* **2009**, *131*, 14136.
[37] S. D. Feyter, F. C. D. Schryver, *Chem. Soc. Rev.* **2003**, *32*, 139.
[38] X. Liu, C. Guan, D. Wang, L. Wan, *Advanced Materials* **2014**, *26*, 6912.
[39] R. Gutzler, *Phys. Chem. Chem. Phys.* **2016**, *18*, 29092.
[40] S. Furukawa, H. Uji-i, K. Tahara, T. Ichikawa, M. Sonoda, F. C. De Schryver, Y. Tobe, S. De Feyter, *J. Am. Chem. Soc.* **2006**, *128*, 3502.
[41] K. Tahara, S. Furukawa, H. Uji-i, T. Uchino, T. Ichikawa, J. Zhang, W. Mamdouh, M. Sonoda, F. C. De Schryver, S. De Feyter, Y. Tobe, *J. Am. Chem. Soc.* **2006**, *128*, 16613.
[42] X. Huang, S. Zhang, L. Liu, L. Yu, G. Chen, W. Xu, D. Zhu, *Angewandte Chemie International Edition* **2018**, *57*, 146.
[43] L. Dong, Y. Kim, D. Er, A. M. Rappe, V. B. Shenoy, *Phys. Rev. Lett.* **2016**, *116*, 096601.
[44] T. Deng, W. Shi, Z. M. Wong, G. Wu, X. Yang, J.-C. Zheng, H. Pan, S.-W. Yang, *J. Phys. Chem. Lett.* **2021**, *12*, 6934.
[45] Y. Yin, Y. Gao, L. Zhang, Y.-Y. Zhang, S. Du, *Sci. China Mater.* **2024**, *67*, 1202.
[46] M. G. Yamada, H. Fujita, M. Oshikawa, *Phys. Rev. Lett.* **2017**, *119*, 057202.
[47] Y.-P. Mo, X.-H. Liu, D. Wang, *ACS Nano* **2017**, *11*, 11694.
[48] H. Zhou, H. Dang, J.-H. Yi, A. Nanci, A. Rochefort, J. D. Wuest, *J. Am. Chem. Soc.* **2007**, *129*, 13774.
[49] F. Haase, B. V. Lotsch, *Chem. Soc. Rev.* **2020**, *49*, 8469.
[50] J. Tu, W. Song, B. Chen, Y. Li, L. Chen, *Chemistry A European J* **2023**, *29*, e202302380.
[51] U. Schlickum, R. Decker, F. Klappenberger, G. Zoppellaro, S. Klyatskaya, W. Auwärter, S. Neppl, K. Kern, H. Brune, M. Ruben, J. V. Barth, *J. Am. Chem. Soc.* **2008**, *130*, 11778.
[52] C. Deng, J. Wang, H. Zhu, C. Xu, X. Fan, Y. Wen, P. Huang, H. Lin, Q. Li, L. Chi, *J. Phys. Chem. Lett.* **2023**, *14*, 9584.
[53] W. Pan, C. Mützel, S. Haldar, H. Hohmann, S. Heinze, J. M. Farrell, R. Thomale, M. Bode, F. Würthner, J. Qi, *Angew Chem Int Ed* **2024**, *63*, e202400313.

[54] M. Pan, X. Zhang, Y. Zhou, P. Wang, Q. Bian, H. Liu, X. Wang, X. Li, A. Chen, X. Lei, S. Li, Z. Cheng, Z. Shao, H. Ding, J. Gao, F. Li, F. Liu, *Phys. Rev. Lett.* **2023**, *130*, 036203.
[55] K. I. Shivakumar, S. Noro, Y. Yamaguchi, Y. Ishigaki, A. Saeki, K. Takahashi, T. Nakamura, I. Hisaki, *Chemical Communications* **2021**, *57*, 1157.
[56] P. Tholen, C. A. Peeples, R. Schaper, C. Bayraktar, T. S. Erkal, M. M. Ayhan, B. Çoşut, J. Beckmann, A. O. Yazaydin, M. Wark, G. Hanna, Y. Zorlu, G. Yücesan, *Nat Commun* **2020**, *11*, 3180.
[57] C.-H. Liu, A. Wei, M. F. Cheung, D. F. Perepichka, *Chem. Mater.* **2022**, *34*, 3461.
[58] Y. Jing, T. Heine, *J. Am. Chem. Soc.* **2019**, *141*, 743.
[59] T. Hu, T. Zhang, H. Mu, Z. Wang, *J. Phys. Chem. Lett.* **2022**, *13*, 10905.
[60] G. Galeotti, F. De Marchi, E. Hamzehpoor, O. MacLean, M. Rajeswara Rao, Y. Chen, L. V. Besteiro, D. Dettmann, L. Ferrari, F. Frezza, P. M. Sheverdyaeva, R. Liu, A. K. Kundu, P. Moras, M. Ebrahimi, M. C. Gallagher, F. Rosei, D. F. Perepichka, G. Contini, *Nat. Mater.* **2020**, *19*, 874.
[61] R. Pawlak, X. Liu, S. Ninova, P. D'Astolfo, C. Drechsel, J. Liu, R. Häner, S. Decurtins, U. Aschauer, S. Liu, E. Meyer, *Angew Chem Int Ed* **2021**, *60*, 8370.
[62] Z. Shi, N. Lin, *J. Am. Chem. Soc.* **2009**, *131*, 5376.
[63] M. Hua, B. Xia, M. Wang, E. Li, J. Liu, T. Wu, Y. Wang, R. Li, H. Ding, J. Hu, Y. Wang, J. Zhu, H. Xu, W. Zhao, N. Lin, *J. Phys. Chem. Lett.* **2021**, *12*, 3733.
[64] L. Z. Zhang, Z. F. Wang, B. Huang, B. Cui, Z. Wang, S. X. Du, H.-J. Gao, F. Liu, *Nano Lett.* **2016**, *16*, 2072.
[65] J. Wang, Y. Zheng, X. Nie, C. Xu, Z. Hao, L. Song, S. You, J. Xi, M. Pan, H. Lin, Y. Li, H. Zhang, Q. Li, L. Chi, *J. Phys. Chem. Lett.* **2021**, *12*, 8151.
[66] L. Dong, Z. Gao, N. Lin, *Progress in Surface Science* **2016**, *91*, 101.
[67] W. P. Lustig, S. Mukherjee, N. D. Rudd, A. V. Desai, J. Li, S. K. Ghosh, *Chem. Soc. Rev.* **2017**, *46*, 3242.
[68] T. Takenaka, K. Ishihara, M. Roppongi, Y. Miao, Y. Mizukami, T. Makita, J. Tsurumi, S. Watanabe, J. Takeya, M. Yamashita, K. Torizuka, Y. Uwatoko, T. Sasaki, X. Huang, W. Xu, D. Zhu, N. Su, J.-G. Cheng, T. Shibauchi, K. Hashimoto, *Sci. Adv.* **2021**, *7*, eabf3996.
[69] H. Furukawa, K. E. Cordova, M. O'Keeffe, O. M. Yaghi, *Science* **2013**, *341*, 1230444.
[70] Z. Fu, Y. Zhang, M. Jia, S. Zhang, L. Guan, D. Xing, J. Tao, *Phys. Chem. Chem. Phys.* **2024**, *26*, 21767.
[71] E. Coronado, *Nat Rev Mater* **2020**, *5*, 87.

[72] B. Field, A. Schiffrin, N. V. Medhekar, *npj Comput Mater* **2022**, *8*, 227.
[73] Q. Yu, D. Wang, *J. Mater. Chem. A* **2023**, *11*, 5548.
[74] D. Kumar, J. Hellerstedt, B. Field, B. Lowe, Y. Yin, N. V. Medhekar, A. Schiffrin, *Adv Funct Materials* **2021**, *31*, 2106474.
[75] N. Su, W. Jiang, Z. Wang, F. Liu, *Applied Physics Letters* **2018**, *112*, 033301.
[76] L. Liu, B. Zhao, J. Zhang, H. Bao, H. Huan, Y. Xue, Y. Li, Z. Yang, *Phys. Rev. B* **2021**, *104*, 245414.
[77] X. Zhang, Y. Zhou, B. Cui, M. Zhao, F. Liu, *Nano Lett.* **2017**, *17*, 6166.
[78] Y. Zhang, J. Lu, W. Gao, Y. Zhang, N. Li, S. Li, G. Niu, B. Fu, L. Gao, J. Cai, *Chin. J. Chem.* **2024**, cjoc.202400557.
[79] T. Wang, Q. Fan, L. Feng, Z. Tao, J. Huang, H. Ju, Q. Xu, S. Hu, J. Zhu, *ChemPhysChem* **2017**, *18*, 3329.
[80] I. Piquero‐Zulaica, W. Hu, A. P. Seitsonen, F. Haag, J. Küchle, F. Allegretti, Y. Lyu, L. Chen, K. Wu, Z. M. A. El‐Fattah, E. Aktürk, S. Klyatskaya, M. Ruben, M. Muntwiler, J. V. Barth, Y. Zhang, *Advanced Materials* **2024**, 2405178.
[81] B. Field, *npj Computational Materials* **2022**.
[82] B. Lowe, B. Field, J. Hellerstedt, J. Ceddia, H. L. Nourse, B. J. Powell, N. V. Medhekar, A. Schiffrin, *Nat Commun* **2024**, *15*, 3559.
[83] L. Yan, O. J. Silveira, B. Alldritt, O. Krejčí, A. S. Foster, P. Liljeroth, *Adv. Funct. Mater.* **2021**.
[84] L. Yan, O. J. Silveira, B. Alldritt, S. Kezilebieke, A. S. Foster, P. Liljeroth, *ACS Nano* **2021**, *15*, 17813.
[85] C. Lyu, Y. Gao, K. Zhou, M. Hua, Z. Shi, P.-N. Liu, L. Huang, N. Lin, *ACS Nano* **2024**, *18*, 19793.
[86] Y. Yang, B. Liang, J. Kreie, M. Hambsch, Z. Liang, C. Wang, S. Huang, X. Dong, L. Gong, C. Liang, D. Lou, Z. Zhou, J. Lu, Y. Yang, X. Zhuang, H. Qi, U. Kaiser, S. C. B. Mannsfeld, W. Liu, A. Gölzhäuser, Z. Zheng, *Nature* **2024**, *630*, 878.
[87] K. Liu, H. Qi, R. Dong, R. Shivhare, M. Addicoat, T. Zhang, H. Sahabudeen, T. Heine, S. Mannsfeld, U. Kaiser, Z. Zheng, X. Feng, *Nat. Chem.* **2019**, *11*, 994.
[88] D. M. Eigler, E. K. Schweizer, *Nature* **1990**, *344*, 524.
[89] M. F. Crommie, C. P. Lutz, D. M. Eigler, *Nature* **1993**, *363*, 524.
[90] I. Piquero-Zulaica, J. Lobo-Checa, Z. M. A. El-Fattah, J. E. Ortega, F. Klappenberger, W. Auwärter, J. V. Barth, *Rev. Mod. Phys.* **2022**, *94*, 045008.
[91] J. L. Zhang, S. Zhao, S. Sun, H. Ding, J. Hu, Y. Li, Q. Xu, X. Yu, M. Telychko, J. Su, C. Gu, Y. Zheng, X. Lian, Z. Ma, R. Guo, J. Lu, Z. Sun, J. Zhu, Z. Li, W. Chen, *ACS Nano* **2020**, *14*, 3687.

[92] H. Tian, J.-Q. Zhang, W. Ho, J.-P. Xu, B. Xia, Y. Xia, J. Fan, H. Xu, M. Xie, S. Y. Tong, *Matter* **2020**, *2*, 111.
[93] S. Sun, S. Zhao, Y. Z. Luo, X. Gu, X. Lian, A. Tadich, D.-C. Qi, Z. Ma, Y. Zheng, C. Gu, J. L. Zhang, Z. Li, W. Chen, *Nano Lett.* **2020**, *20*, 5583.
[94] K. K. Gomes, W. Mar, W. Ko, F. Guinea, H. C. Manoharan, *Nature* **2012**, *483*, 306.
[95] S. Wang, L. Z. Tan, W. Wang, S. G. Louie, N. Lin, *Phys. Rev. Lett.* **2014**, *113*, 196803.
[96] M. R. Slot, T. S. Gardenier, P. H. Jacobse, *NATURE PHYSICS* **2017**, *13*.
[97] S. N. Kempkes, M. R. Slot, J. J. van den Broeke, P. Capiod, W. A. Benalcazar, D. Vanmaekelbergh, D. Bercioux, I. Swart, C. Morais Smith, *Nat. Mater.* **2019**, *18*, 1292.
[98] F. E. Kalff, M. P. Rebergen, E. Fahrenfort, J. Girovsky, R. Toskovic, J. L. Lado, J. Fernández-Rossier, A. F. Otte, *Nature Nanotech* **2016**, *11*, 926.
[99] S. Fölsch, J. Yang, C. Nacci, K. Kanisawa, *Phys. Rev. Lett.* **2009**, *103*, 096104.
[100] K. Sagisaka, D. Fujita, *Applied Physics Letters* **2006**, *88*, 203118.
[101] V. D. Pham, Y. Pan, S. C. Erwin, S. Fölsch, *Phys. Rev. Research* **2024**, *6*, 013269.
[102] A. A. Khajetoorians, *NATURE PHYSICS* **2012**, *8*.
[103] C. F. Hirjibehedin, C. P. Lutz, A. J. Heinrich, *Science* **2006**, *312*, 1021.
[104] S. E. Freeney, M. R. Slot, T. S. Gardenier, I. Swart, D. Vanmaekelbergh, *ACS Nanosci. Au* **2022**, *2*, 198.
[105] Q. Tian, S. Izadi Vishkayi, M. Bagheri Tagani, L. Zhang, Y. Tian, L.-J. Yin, L. Zhang, Z. Qin, *Nano Lett.* **2023**, *23*, 9851.
[106] L. Huang, X. Kong, Q. Zheng, Y. Xing, H. Chen, Y. Li, Z. Hu, S. Zhu, J. Qiao, Y.-Y. Zhang, H. Cheng, Z. Cheng, X. Qiu, E. Liu, H. Lei, X. Lin, Z. Wang, H. Yang, W. Ji, H.-J. Gao, *Nat Commun* **2023**, *14*, 5230.
[107] B. He, G. Tian, J. Gou, B. Liu, K. Shen, Q. Tian, Z. Yu, F. Song, H. Xie, Y. Gao, Y. Lu, K. Wu, L. Chen, H. Huang, *Surface Science* **2019**, *679*, 147.
[108] Li T.-X., Key Laboratory of Artificial Structures and Quantum Control (Ministry of Education), Shenyang National Laboratory for Materials Science, School of Physics & Astronomy, Shanghai Jiao Tong University, Shanghai 200240, China, Tsung-Dao Lee Institute, Shanghai Jiao Tong University, Shanghai 201210, China, *Acta Phys. Sin.* **2022**, *71*, 127309.

[109] E. C. Regan, D. Wang, C. Jin, M. I. Bakti Utama, B. Gao, X. Wei, S. Zhao, W. Zhao, Z. Zhang, K. Yumigeta, M. Blei, J. D. Carlström, K. Watanabe, T. Taniguchi, S. Tongay, M. Crommie, A. Zettl, F. Wang, *Nature* **2020**, *579*, 359.
[110] A. Uri, S. Grover, Y. Cao, J. A. Crosse, K. Bagani, D. Rodan-Legrain, Y. Myasoedov, K. Watanabe, T. Taniguchi, P. Moon, M. Koshino, P. Jarillo-Herrero, E. Zeldov, *Nature* **2020**, *581*, 47.
[111] H. Yoo, R. Engelke, S. Carr, S. Fang, K. Zhang, P. Cazeaux, S. H. Sung, R. Hovden, A. W. Tsen, T. Taniguchi, K. Watanabe, G.-C. Yi, M. Kim, M. Luskin, E. B. Tadmor, E. Kaxiras, P. Kim, *Nat. Mater.* **2019**, *18*, 448.
[112] M. R. Rosenberger, H.-J. Chuang, M. Phillips, V. P. Oleshko, K. M. McCreary, S. V. Sivaram, C. S. Hellberg, B. T. Jonker, *ACS Nano* **2020**, *14*, 4550.
[113] F. K. de Vries, J. Zhu, E. Portolés, G. Zheng, M. Masseroni, A. Kurzmann, T. Taniguchi, K. Watanabe, A. H. MacDonald, K. Ensslin, T. Ihn, P. Rickhaus, *Phys. Rev. Lett.* **2020**, *125*, 176801.
[114] Y. Liu, P. Stradins, S.-H. Wei, *Science Advances* **2016**, *2*, e1600069.
[115] Y. Cao, V. Fatemi, S. Fang, K. Watanabe, T. Taniguchi, E. Kaxiras, P. Jarillo-Herrero, *Nature* **2018**, *556*, 43.
[116] Z. Bi, N. F. Q. Yuan, L. Fu, *Phys. Rev. B* **2019**, *100*, 035448.
[117] Y. Cao, V. Fatemi, A. Demir, S. Fang, S. L. Tomarken, J. Y. Luo, J. D. Sanchez-Yamagishi, K. Watanabe, T. Taniguchi, E. Kaxiras, R. C. Ashoori, P. Jarillo-Herrero, *Nature* **2018**, *556*, 80.
[118] K. Tran, G. Moody, F. Wu, X. Lu, J. Choi, K. Kim, A. Rai, D. A. Sanchez, J. Quan, A. Singh, J. Embley, A. Zepeda, M. Campbell, T. Autry, T. Taniguchi, K. Watanabe, N. Lu, S. K. Banerjee, K. L. Silverman, S. Kim, E. Tutuc, L. Yang, A. H. MacDonald, X. Li, *Nature* **2019**, *567*, 71.
[119] C. Jin, E. C. Regan, A. Yan, M. Iqbal Bakti Utama, D. Wang, S. Zhao, Y. Qin, S. Yang, Z. Zheng, S. Shi, K. Watanabe, T. Taniguchi, S. Tongay, A. Zettl, F. Wang, *Nature* **2019**, *567*, 76.
[120] K. L. Seyler, P. Rivera, H. Yu, N. P. Wilson, E. L. Ray, D. G. Mandrus, J. Yan, W. Yao, X. Xu, *Nature* **2019**, *567*, 66.
[121] T. Li, S. Jiang, B. Shen, Y. Zhang, L. Li, Z. Tao, T. Devakul, K. Watanabe, T. Taniguchi, L. Fu, J. Shan, K. F. Mak, *Nature* **2021**, *600*, 641.
[122] M. Serlin, C. L. Tschirhart, H. Polshyn, Y. Zhang, J. Zhu, K. Watanabe, T. Taniguchi, L. Balents, A. F. Young, *Science* **2020**, *367*, 900.
[123] Z. Li, J. Zhuang, L. Wang, H. Feng, Q. Gao, X. Xu, W. Hao, X. Wang, C. Zhang, K. Wu, S. X. Dou, L. Chen, Z. Hu, Y. Du, *Sci. Adv.* **2018**, *4*, eaau4511.

[124] Q. Zheng, C.-Y. Hao, X.-F. Zhou, Y.-X. Zhao, J.-Q. He, L. He, *Phys. Rev. Lett.* **2022**, *129*, 076803.
[125] D. Pei, B. Wang, Z. Zhou, Z. He, L. An, S. He, C. Chen, Y. Li, L. Wei, A. Liang, J. Avila, P. Dudin, V. Kandyba, A. Giampietri, M. Cattelan, A. Barinov, Z. Liu, J. Liu, H. Weng, N. Wang, J. Xue, Y. Chen, *Phys. Rev. X* **2022**, *12*, 021065.
[126] D. Park, C. Park, E. Ko, K. Yananose, R. Engelke, X. Zhang, K. Davydov, M. Green, S. H. Park, J. H. Lee, K. Watanabe, S. M. Yang, K. Wang, P. Kim, Y.-W. Son, H. Yoo, .
[127] Z. Chu, E. C. Regan, X. Ma, D. Wang, Z. Xu, M. I. B. Utama, K. Yumigeta, M. Blei, K. Watanabe, T. Taniguchi, S. Tongay, F. Wang, K. Lai, *Phys. Rev. Lett.* **2020**, *125*, 186803.
[128] X. Huang, T. Wang, S. Miao, C. Wang, Z. Li, Z. Lian, T. Taniguchi, K. Watanabe, S. Okamoto, D. Xiao, S.-F. Shi, Y.-T. Cui, *Nat. Phys.* **2021**, *17*, 715.
[129] X. Huang, L. Chen, S. Tang, C. Jiang, C. Chen, H. Wang, Z.-X. Shen, H. Wang, Y.-T. Cui, *Nano Lett.* **2021**, *21*, 4292.
[130] K. Lee, M. I. B. Utama, S. Kahn, A. Samudrala, N. Leconte, B. Yang, S. Wang, K. Watanabe, T. Taniguchi, M. V. P. Altoé, G. Zhang, A. Weber-Bargioni, M. Crommie, P. D. Ashby, J. Jung, F. Wang, A. Zettl, *Science Advances* **2020**, *6*, eabd1919.
[131] F. M. Arnold, A. Ghasemifard, A. Kuc, J. Kunstmann, T. Heine, *2D Mater.* **2023**, *10*, 045010.
[132] M. Claassen, L. Xian, D. M. Kennes, A. Rubio, *Nat Commun* **2022**, *13*, 4915.
[133] A. P. Reddy, T. Devakul, L. Fu, *Phys. Rev. Lett.* **2023**, *131*, 246501.
[134] M. Angeli, A. H. MacDonald, *Proceedings of the National Academy of Sciences* **2021**, *118*, e2021826118.
[135] H. Li, Z. Xiang, A. P. Reddy, T. Devakul, R. Sailus, R. Banerjee, T. Taniguchi, K. Watanabe, S. Tongay, A. Zettl, L. Fu, M. F. Crommie, F. Wang, *Science* **2024**, *385*, 86.
[136] B. Padhi, C. Setty, P. W. Phillips, *Nano Lett.* **2018**, *18*, 6175.
[137] Z. Liu, X. Kong, Z. Wu, L. Zhou, J. Qiao, W. Ji, *Exotic electronic states in gradient-strained untwisted graphene bilayers*, arXiv, **2023**.
[138] C. R. Woods, F. Withers, M. J. Zhu, Y. Cao, G. Yu, A. Kozikov, M. Ben Shalom, S. V. Morozov, M. M. Van Wijk, A. Fasolino, M. I. Katsnelson, K. Watanabe, T. Taniguchi, A. K. Geim, A. Mishchenko, K. S. Novoselov, *Nat Commun* **2016**, *7*, 10800.
[139] J. D. Sanchez-Yamagishi, T. Taychatanapat, K. Watanabe, T. Taniguchi, A. Yacoby, P. Jarillo-Herrero, *Phys. Rev. Lett.* **2012**, *108*, 076601.

[140] L. Wang, Y. Gao, B. Wen, Z. Han, T. Taniguchi, K. Watanabe, M. Koshino, J. Hone, C. R. Dean, *Science* 2015.
[141] D. Wang, G. Chen, C. Li, M. Cheng, W. Yang, S. Wu, G. Xie, J. Zhang, J. Zhao, X. Lu, P. Chen, G. Wang, J. Meng, J. Tang, R. Yang, C. He, D. Liu, D. Shi, K. Watanabe, T. Taniguchi, J. Feng, Y. Zhang, G. Zhang, *Phys. Rev. Lett.* 2016, *116*, 126101.
[142] W. Zhou, X. Zou, S. Najmaei, Z. Liu, Y. Shi, J. Kong, J. Lou, P. M. Ajayan, B. I. Yakobson, J.-C. Idrobo, *Nano Lett.* 2013, *13*, 2615.
[143] S. Najmaei, Z. Liu, W. Zhou, X. Zou, G. Shi, S. Lei, B. I. Yakobson, J.-C. Idrobo, P. M. Ajayan, J. Lou, *Nature Mater* 2013, *12*, 754.
[144] Y. L. Huang, Y. Chen, W. Zhang, S. Y. Quek, C.-H. Chen, L.-J. Li, W.-T. Hsu, W.-H. Chang, Y. J. Zheng, W. Chen, A. T. S. Wee, *Nat Commun* 2015, *6*, 6298.
[145] H.-P. Komsa, J. Kotakoski, S. Kurasch, O. Lehtinen, U. Kaiser, A. V. Krasheninnikov, *Phys. Rev. Lett.* 2012, *109*, 035503.
[146] A. M. van der Zande, P. Y. Huang, D. A. Chenet, T. C. Berkelbach, Y. You, G.-H. Lee, T. F. Heinz, D. R. Reichman, D. A. Muller, J. C. Hone, *Nature Mater* 2013, *12*, 554.
[147] Y.-C. Lin, T. Björkman, H.-P. Komsa, P.-Y. Teng, C.-H. Yeh, F.-S. Huang, K.-H. Lin, J. Jadczak, Y.-S. Huang, P.-W. Chiu, A. V. Krasheninnikov, K. Suenaga, *Nat Commun* 2015, *6*, 6736.
[148] H. Liu, L. Jiao, F. Yang, Y. Cai, X. Wu, W. Ho, C. Gao, J. Jia, N. Wang, H. Fan, W. Yao, M. Xie, *Phys. Rev. Lett.* 2014, *113*, 066105.
[149] H. Murata, A. Koma, *Phys. Rev. B* 1999, *59*, 10327.
[150] J. Hong, C. Wang, H. Liu, X. Ren, J. Chen, G. Wang, J. Jia, M. Xie, C. Jin, W. Ji, J. Yuan, Z. Zhang, *Nano Lett.* 2017, *17*, 6653.
[151] P. M. Coelho, H.-P. Komsa, H. Coy Diaz, Y. Ma, A. V. Krasheninnikov, M. Batzill, *ACS Nano* 2018, *12*, 3975.
[152] Y. Yu, G. Wang, S. Qin, N. Wu, Z. Wang, K. He, X.-A. Zhang, *Carbon* 2017, *115*, 526.
[153] L. Dong, G.-Y. Wang, Z. Zhu, C.-X. Zhao, X.-Y. Yang, A.-M. Li, J.-L. Chen, D.-D. Guan, Y.-Y. Li, H. Zheng, M.-H. Xie, J.-F. Jia, *Chinese Phys. Lett.* 2018, *35*, 066801.
[154] J. Zhang, Y. Xia, B. Wang, Y. Jin, H. Tian, W. kin Ho, H. Xu, C. Jin, M. Xie, *2D Mater.* 2020, *8*, 015006.
[155] O. Lehtinen, H.-P. Komsa, A. Pulkin, M. B. Whitwick, M.-W. Chen, T. Lehnert, M. J. Mohn, O. V. Yazyev, A. Kis, U. Kaiser, A. V. Krasheninnikov, *ACS Nano* 2015, *9*, 3274.
[156] T. Mori, H. Abe, K. S. K. Saiki, A. K. A. Koma, *Jpn. J. Appl. Phys.* 1993, *32*, 2945.

[157] F. S. Ohuchi, B. A. Parkinson, K. Ueno, A. Koma, *Journal of Applied Physics* **1990**, *68*, 2168.
[158] J. Lin, S. T. Pantelides, W. Zhou, *ACS Nano* **2015**, *9*, 5189.
[159] S. Barja, S. Wickenburg, Z.-F. Liu, Y. Zhang, H. Ryu, M. M. Ugeda, Z. Hussain, Z.-X. Shen, S.-K. Mo, E. Wong, M. B. Salmeron, F. Wang, M. F. Crommie, D. F. Ogletree, J. B. Neaton, A. Weber-Bargioni, *Nature Phys* **2016**, *12*, 751.
[160] H. C. Diaz, Y. Ma, R. Chaghi, M. Batzill, *Applied Physics Letters* **2016**, *108*, 191606.
[161] H. Liu, H. Zheng, F. Yang, L. Jiao, J. Chen, W. Ho, C. Gao, J. Jia, M. Xie, *ACS Nano* **2015**, *9*, 6619.
[162] H. C. Diaz, R. Chaghi, Y. Ma, M. Batzill, *2D Mater.* **2015**, *2*, 044010.
[163] Y. Ma, S. Kolekar, H. Coy Diaz, J. Aprojanz, I. Miccoli, C. Tegenkamp, M. Batzill, *ACS Nano* **2017**, *11*, 5130.
[164] W. Jolie, C. Murray, P. S. Weiß, J. Hall, F. Portner, N. Atodiresei, A. V. Krasheninnikov, C. Busse, H.-P. Komsa, A. Rosch, T. Michely, *Phys. Rev. X* **2019**, *9*, 011055.
[165] M. Batzill, *J. Phys.: Condens. Matter* **2018**, *30*, 493001.
[166] J. Dai, Z. Zhang, Z. Pan, C. Wang, C. Zhang, Z. Cheng, W. Ji, *Kagome bands and magnetism in MoTe$_{2-x}$ kagome monolayers*, arXiv, **2024**.
[167] Z. Pan, W. Xiong, J. Dai, Y. Wang, T. Jian, X. Cui, J. Deng, X. Lin, Z. Cheng, Y. Bai, C. Zhu, D. Huo, G. Li, M. Feng, J. He, W. Ji, S. Yuan, F. Wu, C. Zhang, H.-J. Gao, *Ferromagnetism and correlated insulating states in monolayer Mo33Te56*, arXiv, **2024**.
[168] Y.-H. Lin, C.-J. Chen, N. Kumar, T.-Y. Yeh, T.-H. Lin, S. Blügel, G. Bihlmayer, P.-J. Hsu, *Nano Lett.* **2022**, *22*, 8475.
[169] Z.-M. Zhang, B.-C. Gong, J.-H. Nie, F. Meng, Q. Zhang, L. Gu, K. Liu, Z.-Y. Lu, Y.-S. Fu, W. Zhang, *Nano Lett.* **2023**, *23*, 954.
[170] Q. Wu, W. Quan, S. Pan, J. Hu, Z. Zhang, J. Wang, F. Zheng, Y. Zhang, *Nano Lett.* **2024**, acs.nanolett.4c01526.
[171] S. N. Magonov, P. Zoennchen, H. Rotter, H. J. Cantow, G. Thiele, J. Ren, M. H. Whangbo, *J. Am. Chem. Soc.* **1993**, *115*, 2495.
[172] H. Zhang, Z. Shi, Z. Jiang, M. Yang, J. Zhang, Z. Meng, T. Hu, F. Liu, L. Cheng, Y. Xie, J. Zhuang, H. Feng, W. Hao, D. Shen, Y. Du, *Advanced Materials* **2023**, *35*, 2301790.
[173] Z. Cai, H. Cao, H. Sheng, X. Hu, Z. Sun, Q. Zhao, J. Gao, S. Ideta, K. Shimada, J. Huang, P. Cheng, L. Chen, Y. Yao, S. Meng, K. Wu, Z. Wang, B. Feng, *Nano Lett.* **2024**, acs.nanolett.4c02580.
[174] X. Xu, X. Wang, S. Yu, C. Wang, G. Liu, H. Li, J. Yang, J. Li, T. Sun, X. Hai, L. Li, X. Liu, Y. Zhang, W. Zhang, Q. Zhang, K. Wang, N. Xu, Y. Ma, F. Ming, P. Cui, J. Lu, Z. Zhang, X. Xiao, *High-density*

single-atom electrocatalytic centers on two-dimensional topological platinum tellurides with Te-vacancy superstructure, arXiv, **2024**.
[175] H. Zhang, Q. Liu, L. Deng, Y. Ma, S. Daneshmandi, C. Cen, C. Zhang, P. M. Voyles, X. Jiang, J. Zhao, C.-W. Chu, Z. Gai, L. Li, *Nano Lett.* **2024**, *24*, 122.
[176] B. Zhu, W. Huang, H. Lin, H. Feng, K. Palotás, J. Lv, Y. Ren, R. Ouyang, F. Yang, *J. Am. Chem. Soc.* **2024**, *146*, 15887.
[177] Q. Liu, N. Han, S. Zhang, J. Zhao, F. Yang, X. Bao, *Nano Res.* **2018**, *11*, 5957.
[178] W. Huang, Q. Liu, Z. Zhou, Y. Li, Y. Ling, Y. Wang, Y. Tu, B. Wang, X. Zhou, D. Deng, B. Yang, Y. Yang, Z. Liu, X. Bao, F. Yang, *Nat Commun* **2020**, *11*, 2312.
[179] S. Wang, Z. Zhan, X. Fan, Y. Li, P. A. Pantaleón, C. Ye, Z. He, L. Wei, L. Li, F. Guinea, S. Yuan, C. Zeng, *Phys. Rev. Lett.* **2024**, *133*, 066302.
[180] Y. Chen, S. Xu, Y. Xie, C. Zhong, C. Wu, S. B. Zhang, *Phys. Rev. B* **2018**, *98*, 035135.
[181] S. Xing, T. Zhao, J. Zhou, Z. Sun, *J. Phys. Chem. C* **2024**, *128*, 2618.
[182] H. Zhou, M. dos Santos Dias, Y. Zhang, W. Zhao, S. Lounis, *Nat Commun* **2024**, *15*, 4854.
[183] D. Lee, K.-H. Jin, F. Liu, H. W. Yeom, *Nano Lett.* **2022**, *22*, 7902.
[184] M. G. Scheer, B. Lian, *Phys. Rev. Lett.* **2023**, *131*, 266501.
[185] J. Jung, Y.-H. Kim, *Phys. Rev. B* **2022**, *105*, 085138.
[186] A. Olariu, P. Mendels, F. Bert, F. Duc, J. C. Trombe, M. A. de Vries, A. Harrison, *Phys. Rev. Lett.* **2008**, *100*, 087202.
[187] M. P. Shores, E. A. Nytko, B. M. Bartlett, D. G. Nocera, *J. Am. Chem. Soc.* **2005**, *127*, 13462.
[188] L. Balents, *Nature* **2010**, *464*, 199.